

DIRAC MATERIAL GRAPHENE

Elena F. Sheka

Russian Peoples' Friendship University of Russia Moscow, 117198 Russia

Received: May 17, 2017

Abstract. The paper presents an overview of graphene electronic structure in light of a general concept of emergent phenomena that result from the quantum phase transition caused by continuous symmetry breaking. In the current case, the spin symmetry breaking is provided by a drastic enhancement of p_z odd electron correlation when the shortest distance between them, defined by C=C bond length, exceeds critical value R_{crit} . The UHF formalism clearly evidences the broken symmetry occurrence and perfectly suits to self-consistent description of the issue. Empirically supported and convincingly certified, the UHF emergents, such as (i) open-shell character of electron spinorbitals; (ii) spin polarization of electron spectrum; (iii) spin contamination; (iv) depriving the spin multiplicity of electronic states; (v) local spin pool at zero total spin density, and so forth greatly extend the view on ground states of graphene and other sp^2 nanocarbons and not only give a clear vision of spin peculiarities of graphene chemistry but predicatively point to the occurrence of emergents related to graphene physics, such as ferromagnetism, superconductivity and topological nontriviality. The paper presents numerous experimental evidences supporting a deep interrelationship between emergent chemistry and emergent physics of graphene.

1. INTRODUCTION

It has become customary to open each new publication concerning graphene by referring to a standard set of unique applications, awaiting graphene, as the main motivation of performed studies, including fundamental ones as well. The fact seems a normal reaction to the unprecedentedly dense flux of papers of still irreducible number, on the one hand, and exclusively wide range of covered topics of interest, on the other. Apparently, the reference might serve the only restrictive spell code that opens the entrance to the area of an unbelievable mixing the scientific disciplines, methods, goals and results of research. In its turn, a huge mass of information related to fundamental sciences has clearly evidenced the outstanding significance of graphene, having been so far the only object capable to unite natural sciences from mathematics to geology. At the same time, the amount of information, which is not under force to understand in full to any thinking

person, inevitably gives rise to the division of the science of graphene into separate branches, such as the physics of graphene, its chemistry, biophysics, biomedicine, and so forth. Therewith, graphene keeps its uniqueness in all of them exhibiting an exciting universality. If the same graphene is in service to all these branches, there is a time to ask ourselves what is the reason of this universal uniqueness. The first attempt to answer the question is presented in the current paper.

The peculiarity, which may form the ground of the universal uniqueness of a many-electron system, evidently concerns the alteration of its fundamental properties, primarily, continuous symmetry breaking, spin symmetry first and time and space symmetry in the second place. For the first time, the question of the strong influence of a broken symmetry on the behavior of a many-electron system was raised in the P. Anderson famous work "*More is Different*" in 1972 [1] and then supported by other

Corresponding author: Elena F. Sheka, e-mail: sheka@icp.ac.ru

prominent physicists [2-5]. The question was posed theoretically and concerned peculiarities of the solution of many-electron Hamiltonians, particularly, Hartree-Fock (HF) one. The problem arises when the standard symmetric restricted HF (RHF) solutions do not fit the physical reality and are replaced by unrestricted HF (UHF) approach. The replacement concerns the manner of wave function (wf) presentation keeping the Hamiltonian unchanged. The problem stems from the fact that UHF, being eigenfunctions of both electron Hamiltonian and spin projection S_z operator, may either do or do not play this role for spin square operator \hat{S}^2 , just causing spin symmetry breaking in the latter case. The functions are resulted from the implementation of Löwdin's idiom "different orbitals for different spins" and took into account electron correlation in the considered electronic system [6]. The difference of the broken symmetry UHF solution from the spin symmetric RHF one consists in lowering energy $\Delta E^{RU} = E^{UHF} - E^{RHF} < 0$ and a remarkable spin contamination ($\Delta \hat{S}^2 = \hat{S}_{UHF}^2 - \hat{S}_{exact}^2$). The latter, which casts doubts on the purity of spin multiplicity of the system ground state, quite often is attributed to the method disadvantage that leads to erroneous results (see [7,8] and references therein). At the same time, the feature is usually accepted as indication to enhanced electron correlation that requires configuration interaction (CI) schemes for a proper description. There has been a perception, that if UHF approach as the first stage of the CI ones would have been improved towards a complete CI theory, one would expect a deductive restoration of the symmetry and the removing of spin contamination. However, as was pointed by the R. Laughlin in his Nobel lecture in 1999 [3], the symmetry restoration is under question. Actually, "... if the system contains a thermodynamically large number of particles it can happen that a small change to the equations of motion results in a violent rearrangement of the ground state and low-lying excitations and a corresponding breakdown of the one-to-one mapping. This is a quantum phase transition. We say that two states are the same phase of matter if they can be slowly transformed into each other without encountering a quantum phase transition, and different phases of matter if they cannot". In full accordance with the said, there might be two situations concerning UHF breaking of spin symmetry: the expectation of the symmetry restoration, assured by passing to spin-projected of higher levels of the CI theory and the recognition of the fact of the symmetry breaking and the occurrence of quantum phase transition in the electron system under considera-

tion. The first case is actually met for small systems (see [5,9] and references therein). Large systems are more tolerant to symmetry breaking and quantum phase transition that accompanies the latter [1-5] due to which the UHF solution becomes a good approximation of the system ground state. At the same time, the glossary of terms of the new ground state is unavoidably enriched with new ones, sometimes attributed to new 'order parameters' [5], which indicate new properties, acquired by the electron system and nominated as *emergents*. The UHF emergents concern spin polarization of electron states, spin contamination, depriving the exact spin multiplicity of electronic states, and spin structure, composed of local spins of the predetermined value related to the relevant atom as well as many others resulted from the above mentioned.

The emergent character of the ground state has a direct attitude to graphene. Empirically divided into micro (nano) and macro-scale, graphene samples are grouped in two large pools characterized by non-quantized (molecular) and quantized (crystalline) electronic properties, respectively. The two pools are graphene materials providing low-performance and high-performance applications [10]. Since symmetry breaking does not depend on concrete details related to each particular sample [1-5], it is the universal property of the whole graphene family and provides a reliable guide over the ocean of available facts and observations looking for common emergent phenomena characteristic for studied properties.

The current paper presents the first such traveling revealing that broken symmetry unites peculiar spin-dependent chemical properties of graphene molecules, including its mechanochemistry, topochemistry, and biomedicine, with spin-dependent physical properties of crystals, such as ferromagnetism, superconductivity and topological non-triviality.

2. UHF EMERGENTS OF GRAPHENE MOLECULES

Besides the emergents pointed in the previous section, UHF algorithm generates some others, among which there is one concerning the division of molecules into two types, namely, closed-shell and open-shell ones. Belonging to one the types is determined by the internal electronic and structural properties of molecules. Relating to sp^2 nanocarbons, the quantum phase transition from closed-shell to open-shell molecules occurs when the nearest via bond distance between p_z odd elec-

trons exceeds a critical value $R_{\text{crit}}=1.395 \text{ \AA}$ [11]. Open-shell molecules can be conventionally attributed to static and dynamic ones. First type covers species with multiple covalent bonds, such as fullerenes, carbon nanotubes, and graphene [12]. All the outlined molecules are characterised by equilibrium C=C distances, a predominant majority of which exceed R_{crit} . The second type is related to species under stretching that causes elongation and contraction of covalent bonds. UHF approach confidently fixes the classification.

As mentioned earlier, the question of the restoration of continuous symmetry when applying higher approximations of the CI theory to broken symmetry of open-shell molecules has been raised more than once. However, computational and empirical evidences fully discard these expectations in the case of sp^2 nanocarbons. Thus, an experiment has been performed just recently for 14 polyaromatic hydrocarbons (PAH) by using a number of different CI approaches such as UHF, UMP2, QCISD(T), and UDFT [13]. Calculations evidenced that PAH are open-shell molecules starting with naphthalene. Moreover, results, concerning spin contamination $\Delta\hat{S}^2$ of these molecules, occurred to be well consistent for the first three techniques while those of UDFT were practically nil when the UHF ones deviate from the higher approaches of the CI theory no more than $\sim 10\%$. Once wf-based, HF consideration is evidently preferential since the DFT one is much less adapted to the consideration of delicate peculiarities connected with the correlation of electron of different spins.

Each UHF wf generates a nonvanishing spin density matrix and its real and imaginary parts give the spin density and spin current densities producing the relevant UHF spin structure [14]. The structure components are presented by the total number of effectively unpaired electrons N_D and their fractional number on each atom N_{DA} [15-17]. For traditional singlet states with $N_\alpha = N_\beta$, $N_D = 2\Delta\hat{S}^2$, thus becoming a quantitative measure of electron correlation. Both quantities are amenable to computational and experimental verification. Addressing the former for a set of PAHs (see overview in [18] and references therein) revealed the following: (i) the calculated N_D values, obtained by using UHF and density matrix renormalization group (DMRG) algorithms, are practically identical; (ii) the obtained close-to-linear $N_D(n)$ dependence perfectly explains the hampered availability of longer PAHs, with pentacene ($n=5$) being the largest well-characterized acene. The higher acenes are very reactive due to which to overcome the stability problems spe-

cies have to be functionalized by adding protecting groups which inhibit their native high reactivity. In addition to the indirect N_D manifestation discussed above, the last decade has provided convincing direct evidences of the existence by scanning its N_{DA} fractions over the open-shell molecule atoms by noncontact atomic force microscopy (AFM) with a carbon monoxide (CO)-functionalized tip (see [19-21] and references therein). Pentacene as well as sets of olympicenes and triangulenes form the main part of the pool of molecules, consisting of condensed benzenoid units, studied by now. The obtained AFM image maps of the molecules, clearly distinguishing atoms with the highest and lowest strength of the interaction with the oxygen-atom tip, perfectly correlate with the calculated N_{DA} image map exhibiting 'chemical portrait' of the molecules [18]. Happily, such a justification is available now for ($n,3$) graphene nanoribbon as well [22]. As in the case of pentacene, AFM with a CO-terminated tip image (Fig. 1a) is in good consent with the calculated map of the (15, 3) NGr molecule (Fig. 1b) thus evidently justifying a peculiar two-zone character of the graphene pool of effectively unpaired electrons.

The last fraction of the text above should convince that the UHF features of sp^2 nanocarbons are a physical reality due to which broken-spin-symmetry states are stable enough to fit conditions of the molecules ground states.

3. LOCAL SPINS IN GRAPHENE MOLECULE LANDSCAPE

Local spins of graphene, which are associated with effectively unpaired p_z odd electrons, are one of the most important emergents of the UHF formalism applied to the graphene molecule open-shell ground state [18]. As seen in Table 1, bare graphene molecules are characterized by rather big total numbers of such electrons N_D that constitute more than one third of the total number of p_z electrons. It means that the molecules are strongly radicalized thus exhibiting a large chemical activity. Table 1 lists sets of three criterial quantities: ΔE^{Ru} , $\Delta\hat{S}^2$ and N_D , which characterize any open-shell molecule [24]. The data were evaluated for a number of graphene molecules presented by bare rectangular (n_a, n_z) fragments (n_a and n_z count the benzenoid units along armchair and zigzag edges of the fragment, respectively). Consequently, the table as a whole presents the size dependence of the UHF emergents of the graphene molecules. As seen in the table, the parameters are certainly not zero, obviously greatly depending on the fragment size. It should be added

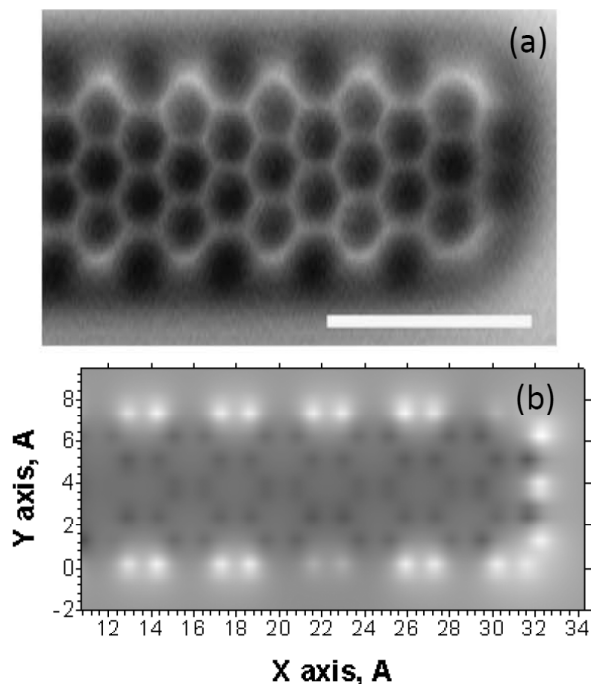


Fig. 1. (a) Constant-height high-resolution AFM image of the zigzag end of a graphene nanoribbon obtained with a CO-terminated tip. White scale bar: 1 nm. Adapted from Ref. 22. (b) ACS N_{DA} image map of the zigzag-end (15,3) NGr molecule with bare edges. UHF AM1 calculations.

as well that the relation $N_D = 2\Delta\hat{S}^2$, which is characteristic for singlet state, is rigidly kept over all the molecules. While the total number of effectively unpaired electrons is the quantitative measure of the activity of whole molecule, or *molecular chemical susceptibility* (MCS) introduced in [25], their partitioning over molecule atoms describes the *atomic chemical susceptibility* (ACS) in terms of N_{DA} due to which image maps of the latter value distribution over atoms present chemical portrait of the associated molecules as well as discloses the distribution of the relevant local spins [26]. Both MCS

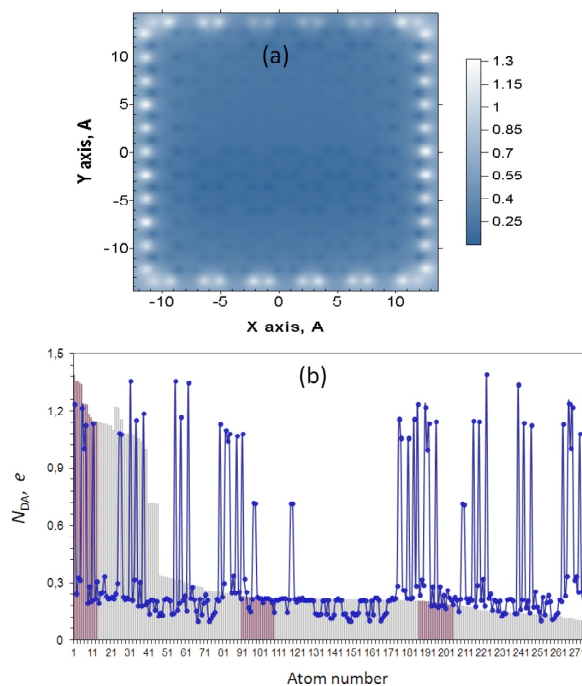


Fig. 2. (a) Equilibrium structure and ACS N_{DA} image map of the (11,11) NGr molecule with bare edges. Scale bar matches N_{DA} values in e. (b) N_{DA} plotting from output file (curve with dots) and max \rightarrow min N_{DA} distribution (histogram). For the first 46 atoms: the histogram reveals first 22 zigzag edge atoms while next 24 bars (from 23 to 46) are related to armchair edge atoms. UHF AM1 calculations.

N_D and ACS N_{DA} are new emergent ‘order parameters’ of open-shell molecules.

The ACS N_{DA} image maps of graphene molecules have a very particular, but therewith standard image which allows both disclosing the local spin distribution over atoms and considering chemical activity of the molecules at the quantitative level. Fig. 2 presents the N_{DA} distribution over atoms of the (11,11) NGr bare molecule. As seen in the figure, according to this parameter, the graphene molecule

Table 1. Identifying parameters of the odd electron correlation in rectangular nanographenes*.

(n_a, n_z) , NGrs	Odd electrons, N_{odd}	ΔE^{RU} , kcal/mol	N_D	$\Delta\hat{S}^2$	J , kcal/mol
(5,5)	88	307	31	15.5	-1.429
(7,7)	150	376	52.6	26.3	-0.888
(9,9)	228	641	76.2	38.1	-0.600
(11,10)	296	760	94.5	47.24	-0.483
(11,12)	346	901	107.4	53.7	-0.406
(15,12)	456	1038	139	69.5	-0.324

*AM1 version of UHF codes of CLUSTER-Z1 [23]. Presented energy values are rounded off to an integer.

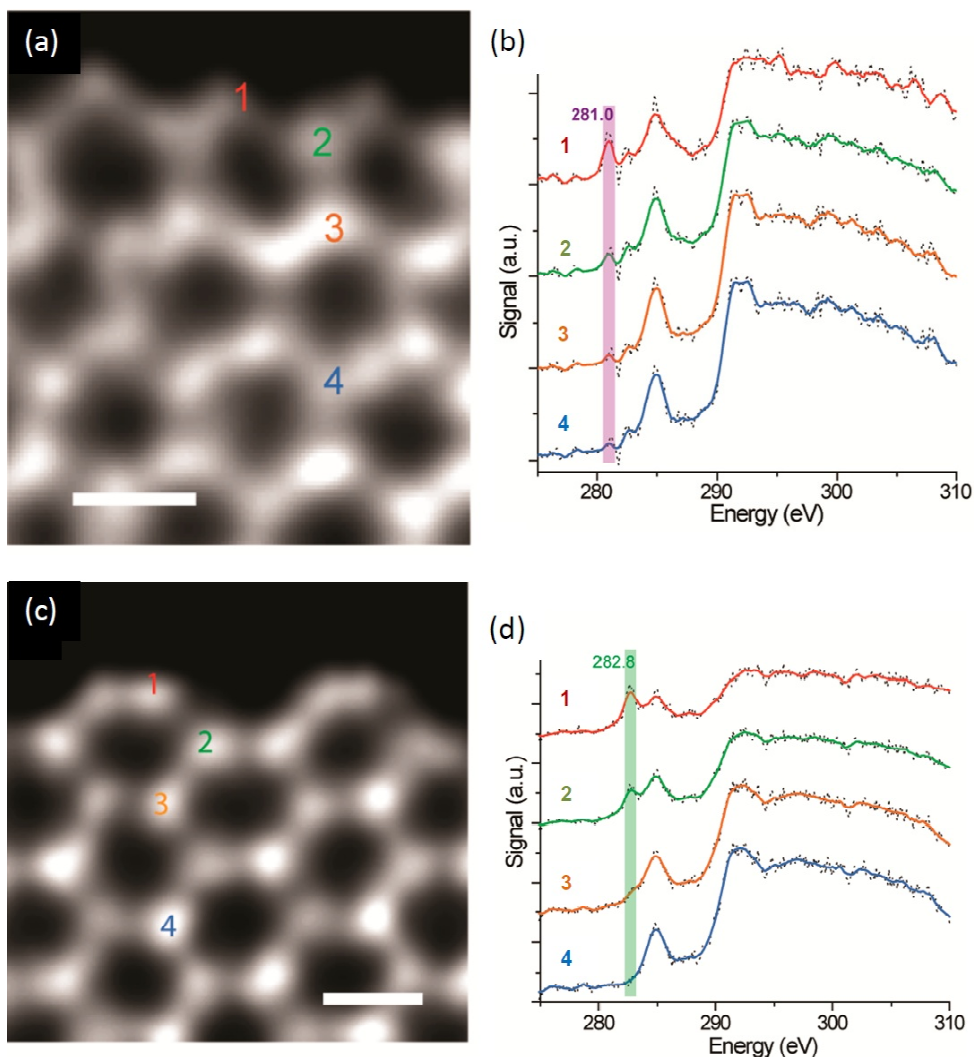


Fig. 3. STEM: EELS mapping of graphene edges. (a) ADF-STEM image and (b) EELS of zigzag edge from the regions numbered in (a). (c) ADF-STEM image and (d) EELS of armchair edge from the regions numbered in (d). White scale bar: 2 Å. Numbers and their colors on ADF-STEM images and EELS spectra coincide. Adapted from Ref. 27.

is definitely divided into two drastically different parts, namely, the circumference involving 46 edge atoms and internal honeycomb zone, or basal plane. Due to six-fold difference of the maximum N_{DA} values in the two areas, the basal plane is practically invisible in Fig. 2a, while keeping a considerable N_{DA} of ~ 0.2 in average. The value rising over the average one occurs only for 40 atoms adjacent the molecule perimeter of edge atoms, for which N_{DA} varies from 0.34 to 0.22. This atom fraction is clearly seen in the histogram in Fig. 2b at atom numbers from 47 to 86.

Presented in the figure is the chemical portrait of the bare (11,11) NGr molecule. As seen from the histogram in Fig. 2b, the chemical activity of the graphene molecule atoms greatly varied within both the circumference and basal plane, more signifi-

cantly within the first one. In the histogram the most intense 46 edge atoms belong to 22 and 24 atoms related to zigzag and armchair edges, respectively. For zigzag atoms N_{DA} values fill the region 1.39-1.10, while the latter for armchair atoms is much wider and constitutes 1.22-0.71. The variety of electron density of carbon atoms along edges of a graphene flake as well as perpendicular to them has been clearly demonstrated just recently by site-specific single-atom electron energy loss spectroscopy (EELS) by using annular dark field (ADF) mode of a low-voltage STEM [27]. Fig. 3 discloses a highly informative picture related to the states of carbon atoms in the vicinity of zigzag and armchair edges. As seen in the figure, the site-dependent peculiarities are observed in the low-energy parts of the EELS spectra, which present K-edges of the carbon EELS

signals. All the low-energy spectra involve a characteristic EELS peak P_b at 285 eV related to the excitation transformation of a core s -electron to an unoccupied σ^* orbital. Additional peaks at 281 eV (P_z) and 282.8 eV (P_a) for the zigzag and armchair edge atoms, respectively, are caused by the s electron excitation to an unoccupied p_z^* orbital and the change to the profile of the EELS is related to variations in the local density of states. The peaks are well pronounced for edge atoms (spectrum 1), significantly decrease in intensity for adjacent atoms (spectrum 2) and practically fully vanish for carbon atoms on the flake basal plane (spectra 3 and 4). Additionally, EELS spectra across the edge markedly vary for both zigzag and armchair atoms. As seen in Fig. 4a, the spectra of two neighboring zigzag atoms (8 and 10) differ so seriously that the peak P_z is substituted by the peak P_a . The latter structure is conserved for the adjacent atom 9, albeit with changing in the intensity distribution between P_a and P_b peaks. EELS spectra in Fig. 4b exhibit the difference in the behavior of the neighboring armchair atoms expressed in changing the P_a/P_b intensities ratio.

The discussed spectral features are well consistent with the conclusion obtained from the above analysis of the N_{DA} distribution in Fig. 2b. Thus, first, the chemical bonding of zigzag and armchair edge atoms is different, bigger in the latter case, which is consistent with lower chemical activity of the armchair edge atoms compared with the zigzag ones. Second, atoms of the adjacent-to-edge rows demonstrate a transient state between the edge and bulk one that well correlates with the activity of 40 adjacent atoms (from 47 to 86) in the histogram in Fig. 2b. Third, inside the region, perimeter of which is formed by adjacent atoms, the carbon atoms can be attributed to the basal-plane ones. Forth, electron density as well as ACS N_{DA} of the edge, adjacent, and bulk atoms significantly varies thus demonstrating that the atom groups are not rigidly standardized and might be very sensitive to external actions due to which graphene molecules are very changeable.

The two-zone electron density image of bare graphene molecule is not news. The feature lays the foundation of a large number of theoretical-computational considerations concerning a particular role of edge atoms in graphene started in 1996 [28] and has been lasting until now (see a collection of papers [29-32] and references therein). The studied graphene objects were mainly pencil-made with a regular honeycomb structure described by standard C=C bonds of 1.42 Å in length and identical

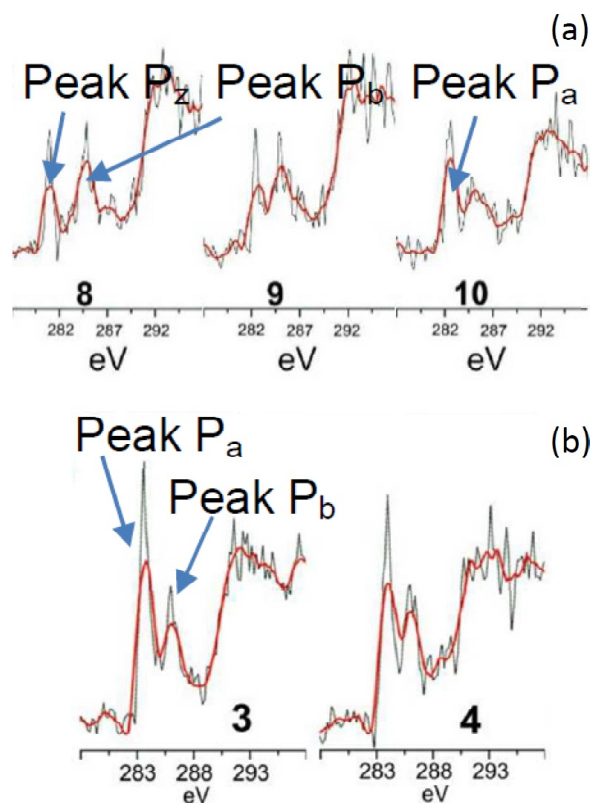


Fig. 4. EELS spectra at the edges of graphene flake. (a) Neighboring zigzag atoms (atoms 8 and 9) and adjacent atom between them (atom 9). (b) Neighboring armchair atoms (atoms 3 and 4). P_z , P_a and P_b match peaks at 281 eV, 282.8 eV, and 285 eV, respectively. Adapted from Ref. 27.

sets of zigzag and armchair edge atoms. The obtained results concern the two-zone electronic structure and the attribution of the edge atoms peculiarity to expected particular magnetic behavior of graphene flakes and, particularly, nanoribbons. However, the latter expectations occurred quite illusive and as shown experimentally, magnetic behavior of graphene samples is not directly connected with peculiar features of their edge atoms. It is worthwhile to remain a skeptical comment of R. Hoffmann concerning his “*Small but Strong Lessons from Chemistry to Nanoscience*” [33]: “*There is a special problem that theory has with unterminated structures—ribbons cut off on the sides, polymers lacking ends. If passivation is not chosen as a strategy, then the radical lobes of the unterminated carbon atoms, or undercoordinated transition metals, will generate states that are roughly in the middle energetically, above filled levels, below empty levels in a typical molecule that has a substantial gap between filled and unfilled levels. If such levels—states, the physicists call them—are not identified as “intruder” states, not really real, but arising from*

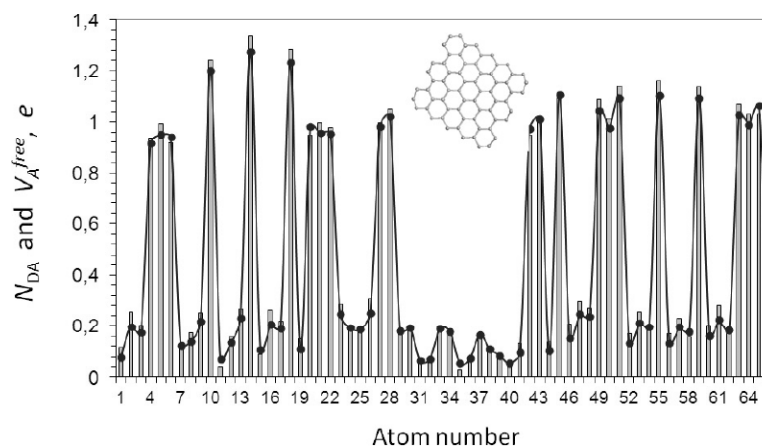


Fig. 5. ACS N_{DA} (histogram) and free valence V_A^{free} (curve with dots) distributions over atoms of the (5,5) NGr molecule. Inset: equilibrium structure of the (5,5) NGr molecule. UHF AM1 calculations.

the artifact of termination, they may be mistaken for real states in the band gap, important electronically. And if electrons are placed in them, there is no end to the trouble one can get into. These band gap states are, of course, the origin of the reactivity of the terminated but not passivated point, line, or plane. But they have little to do with the fundamental electronic structure of the material'.

4. FUNDAMENTALS OF GRAPHENE COMPUTATIONAL SPIN CHEMISTRY

The modern chemistry is strongly occupied by revealing reliable qualitative, better quantitative, descriptors aiming at pointing the consequence of chemical reaction. UHF formalism of open-shell molecules suggests unique quantitative descriptors as emergents MCS N_D and ACS N_{DA} . For molecules with even number of electrons N_{DA} is identical to the atom free valence [34]. Consequently, free valence of atom A, V_A^{free} , is defined as

$$V_A^{\text{free}} = N_V^{\text{val}} - \sum_{B \neq A} K_{AB}. \quad (1)$$

Here N_A^{val} is the number of valence electrons of atom A and $\sum_{B \neq A} K_{AB}$ presents a sum over the generalized bond index

$$K_{AB} = |P_{AB}|^2 + |D_{AB}|^2, \quad (2)$$

where the first term is the Wiberg bond index while the second term is determined by taking into account the spin density matrix. The V_A^{free} distribution (curve with dots) alongside with the ACS N_{DA} (histogram) for the (5,5) NGr molecule is shown in Fig. 5. As seen in the figure, first steps of any chemical reaction occur at the molecule circumference. Since this reactivity area is largely spread in space, the

formation of the first monoderivative does not inhibit the molecule reactivity so that the reaction will continue until the reaction ability is satisfied. This means that any chemical modification of graphene starts as polyderivatization of the pristine molecule at its periphery.

Perfect agreement of N_{DA} and V_A^{free} values shows that the former is actually a quantitative ACS measure and can serve a quantitative descriptor of the molecule target atoms, to which atom-atom contacts are the most desirable in addition reactions. Thus, the values distribution over molecule atoms forms a unique ACS N_{DA} image map, which opens a transparent methodology of a successive algorithmic computational synthesis of any graphene polyderivatives, just selecting the graphene core atom at each step by the largest N_{DA} value. A successive use of this methodology was shown on examples of hydrogenation [35] and oxidation [36] of the (5,5) NGr molecule.

As turned out, already the first addition of any reactant, or modifier, to the edge atom of graphene molecule, chosen by the highest ACS, causes a considerable changing in the pristine ACS N_{DA} image map thus allowing the exhibition of the second edge atom with the highest ACS to proceed with the chemical modification and so forth. Fig. 6 presents a set of (5,5) NGr polyhydrides and polyoxides obtained in the course of the first stage of the relevant per step reactions that concerns framing of the bare molecule. Two important conclusions follow from the figure. First, in spite of seemingly local change of the molecule structure caused by the first addition, the second target carbon atoms does not correspond to the atom that was the second one of the highest activity in the N_{DA} list of the pristine molecule. Second, this atom position as

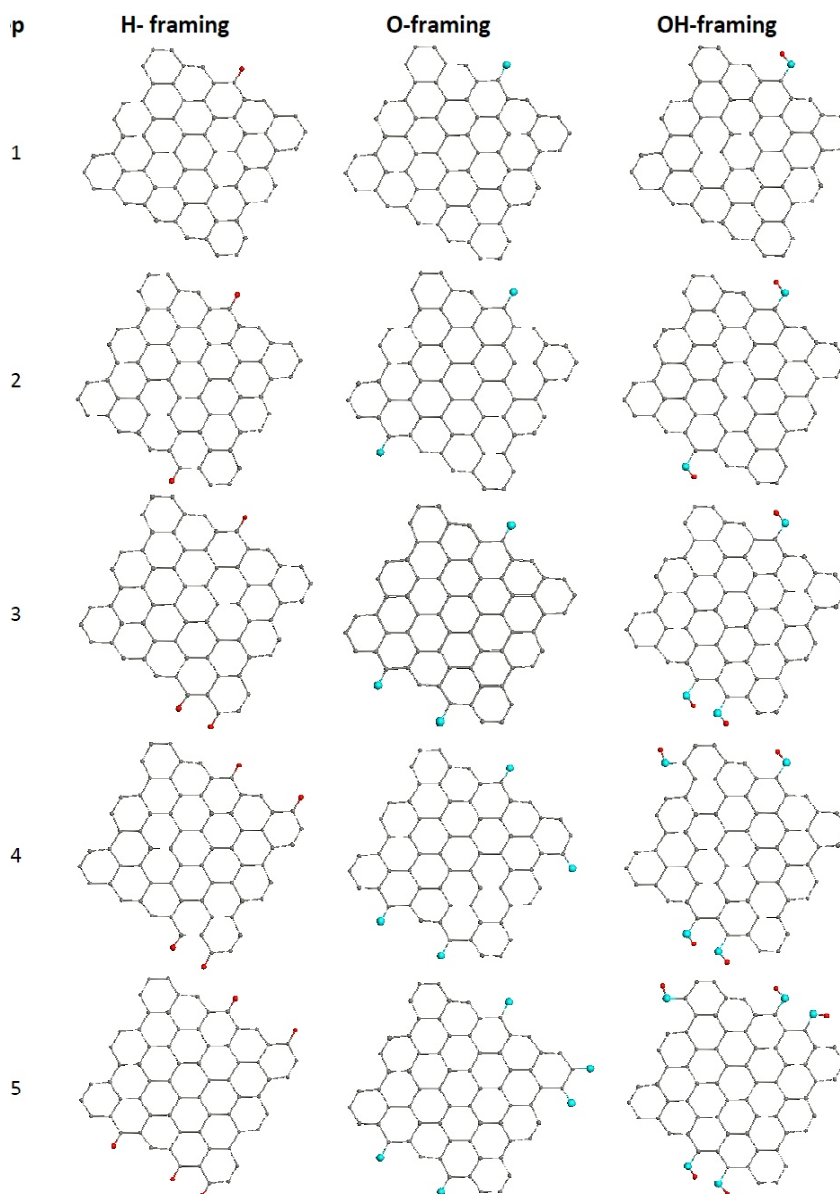


Fig. 6. Equilibrium structures of the (5,5) NGr polyhydrides and polyoxides related to 1st, 2nd, 3rd, 4th, and 5th steps obtained in the course of the relevant stepwise reactions. Gray, blue, and red balls mark carbon, oxygen, and hydrogen atoms, respectively. UHF AM1 calculations.

well as the sequence of next steps varies depending on the chemical nature of the addends. The two features are the result of the redistribution of C=C bond lengths over the molecule thus revealing collective action of its effectively unpaired electrons and/or local spins.

5. NONRELATIVISTIC AND RELATIVISTIC UHF FORMALISM

As we saw in the previous sections, broken spin symmetry, caused by electron correlation, leads to spin mixing revealed as spin contamination $\Delta\hat{S}^2$. However, vectorial spin-orbit coupling (SOC) E^{SO} is

the second reason of the feature due to which we come to the main two issues of the present-day quantum chemistry related to the cooperation of correlation and relativity. It is time to remember an exact expression of W. Liu [37] concerning the topic: “*Only the combination of both relativity and correlation can precisely match experiments that are, without exception, fully relativistic and correlated*”. Important to note another comment of W.Liu that correlation is fully described by the parameterization of the restricted single determinant (RSD) by using a particular method while relativity is in Hamiltonian. The observed course of development of both modern quantum chemistry and relativistic quantum

chemistry [38,39] in the past decade fully confirms the validity of this statement.

The implementation of the first program has resulted in the elaboration of a large set of non-relativistic (NR) methods applied to the consideration of correlation interaction (CI). The General Hartree-Fock (GHF) approach forms a general ground of the series [6] while the UHF formalism is one of the best GHF implementations [40]. The execution of the second program refers us to the Dirac relativistic equation and possible simplifications of its Hamiltonian. Available there is a wide range of relativistic SOC-involved Hamiltonians, which is the result of tremendous efforts of many quantum chemist groups (see a broad discussion of the issue in [38,39,41]). Many of them serve as seamless bridges between the Schrödinger and Dirac equations, which allowed stating that the 'relativity problem' in chemistry has been solved [37]. Certainly, there are still a lot of problems to be solved but the general building of relativistic quantum chemistry (RQC) has been constructed.

To make clear the horizons concerning open-shell molecules, let us consider nonrelativistic QC (NRQC) and RQC approaches on the same UHF footing. The most direct way to incorporate relativistic and correlation effects is to perform the Hartree-Fock calculations employing the Dirac-Coulomb Hamiltonian, but this approach is very difficult and time-consuming. Most studies of relativistic effects have been based upon cruder approximate methods. One of the most successful approach is based on the relativistic effective core potential (RECP) [42]. In this approximation, the relativistic Hamiltonian reads

$$U^{\text{RECP}} = U^{\text{ARECP}} + U^{\text{SO}}. \quad (3)$$

Here relativistic electron potential U^{RECP} is expressed as the sum of the weighted average RECP (ARECP), U^{ARECP} , and the effective one-electron spin-orbit (SO) operator, U^{SO} . When SOC is omitted, RECP becomes ARECP, which is equivalent in form to the effective core potentials in the conventional NR method. Spin-orbit effects can be investigated by performing additional calculations with and without SOC at various levels.

In the case of any HF methods, nonrelativistic wf of the i -th atom is substituted by one-electron molecular spinors with two components (relativistic HF). Consequently, of unrestricted formalism take the form

$$\Psi_i = \begin{pmatrix} \Psi_i^\alpha \\ \Psi_i^\beta \end{pmatrix} \quad (4)$$

for UHF and

$$\Psi_i^+ = \sum_p C_{ip\alpha}^+ \chi_p \alpha + \sum_p C_{ip\beta}^+ \chi_p \beta, \quad (5)$$

$$\Psi_i^- = \sum_p C_{ip\alpha}^- \chi_p \alpha + \sum_p C_{ip\beta}^- \chi_p \beta, \quad (6)$$

for its relativistic analogue. Here α and β refer to spin functions and χ_p is a basis function. The last two equations define a Kramers pair of spinors. When spinors Ψ_i^+ and Ψ_i^- are connected by time-reversal symmetry (analogously to spin symmetric Ψ_i^α and Ψ_i^β of RHF) the relativistic HF method is attributed to the two-component (2c) Kramers restricted Hartree-Fock (KRHF) for polyatomic molecules using RECP with SO operator [42]. When time-reversal symmetry is broken, the pair of spinors (Eq. 5 and Eq.6) defines the (2c) Kramers unrestricted Hartree-Fock (KUHF) method [42, 43]. Analogously to spin symmetry broken Ψ_i^α and Ψ_i^β functions of UHF, the KUHF spinors are referred to as broken Kramers pairs [44]. When SOC is ignored, one may expect practically identical solutions provided by both UHF and KUHF algorithms. Two-component spinors of Eq. (5) and Eq. (6) perfectly serve a basis set of the general complex Hartree-Fock (GCHF) approach [40]. In the framework of the Kramers pair/GCHF approach have been shown that, when applying to an open-shell molecule in the form of unrestricted formalism, the breaking of the Kramers pairs can be characterized by a parameter that is identical to spin contamination of the UHF formalism [44]. The approach was applied, simultaneously with the UHF, to the phenoxyl radical C_6H_5O . As occurred, ΔS^2 constitutes 0.6024, exactly the same for both UHF and KUHF techniques. The results coincidence points to negligibly small SOC effects in this case related to light carbon and oxygen atoms. Additionally, it indicates that in both cases the spin contamination occurs in the result of efficient electron correlation, characteristic for the studied open-shell molecule with the difference that the broken symmetry is spin by nature in the first case when concerns time reversion in the second. Despite the fact the relevant emergents, different by origin, are computationally similar in both cases. This concerns not only spin contamination ΔS^2 but the spin structure as well. Actually, the correlation-stimulated contribution of higher multiplicity determinants with different $\langle \hat{S}^2 \rangle$, but the same $\langle \hat{S}_z \rangle$ expectation value, directly affects the spatial distribution of spin density leading to extra positive and negative density regions, but with no contribution to the overall S_z spin population. The distribution of such a spin density, collinear (COL) with

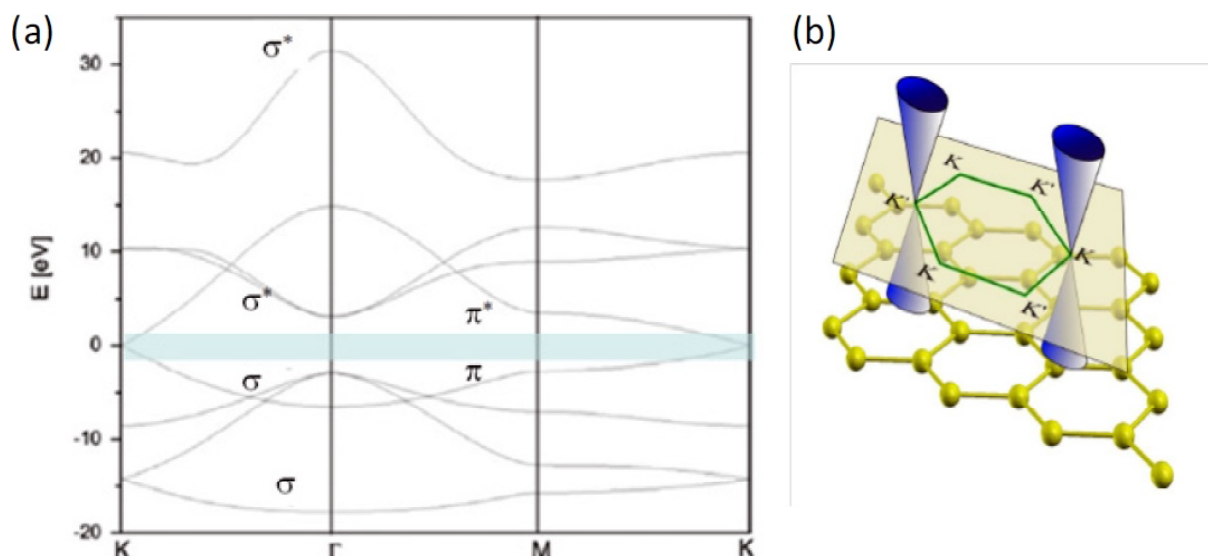


Fig. 7. (a) Widely presented view on the band structure of graphene. Fermi level is settled at zero. The bands below (above) the Fermi level are related to the valence (conductive) zones. (b) Two pairs of valence/conductive Dirac cones at K and K' points at the Fermi level.

magnetic field, and related to the C_6H_5O molecule is fully identical in the case of UHF and KUHF formalisms [44].

6. RELATIVISTIC ELECTRONS OF GRAPHENE CRYSTAL

A tight connection of the UHF emergent phenomena (the KUHF testimony is waiting its time) with C=C bond length distribution is convincingly traced in mechanochemical and topochemical behavior of graphene molecules [45,46] supported with numerous experimental evidences (see [47] and references therein). Taking together and nominated as spin peculiarities, the chemical behavior of graphene molecules strongly evidences broken spin symmetry of the species electronic states, which is greatly challenging to look at physical properties of graphene from this viewpoint as well. However, oriented on determination of electronic band spectrum, the solid-state many-electron approaches to graphene, primarily suggested for graphite, have been developed outside HF formalism, mainly in terms of a simple nearest neighbor tight-binding (TB) approximation [48,49]. Later was shown that the low-energy part of the spectrum closely resembles the Dirac spectrum for massless fermions based on quasi-relativistic consideration [50]. Conceptually, the situation is fully analogous discussed above concerning the solution of Eq. (3) when ignoring SOC. However, if in the case of molecules, nonrelativistic HF approach evidently is much more preferable than relativistic one, the manner of the latter to describe

graphene crystal spectrum turned out more attractive. The approach brought new terms, such as Dirac fermions and Dirac cones, which made graphene physics quasi-relativistic from the very beginning.

The general approximation to electronic band spectrum of graphene does not take into account not only SOC but electron correlation as well and is similar to the RHF approach to molecules supporting any continuous symmetry conservation. The spectrum has a standard image of adjoined Dirac cones at particular points of the Brillouin zone following the symmetry consideration. The consideration proceeds from the fact that graphene primitive cell is simple and contains two atoms. The cells are additionally hexagonally configured to fit the honeycomb lattice, on the one hand, and to provide the hexagonal and flat first Brillouin zone (BZ), on the other. The BZ contains two nonequivalent sets of three vertices K and K' each while Γ point is located at the hexagon centre. In the TB approach is typical to separate the Hamiltonian for π (odd p_z) electrons from that for σ electrons, which is strictly valid only for a flat graphene sheet. Thus obtained, the total band structure of graphene crystal is of particular image, typical view of which is presented in Fig. 7a. Since referring relativistic analogy concerns π bands, it is conventional to just consider the latter. The relevant low-energy quasiparticle states at the Fermi level, marked by a tinny band in the figure, form six pairs of touching cones with the tips at K (K'), two pairs of which are shown in Fig. 7b.

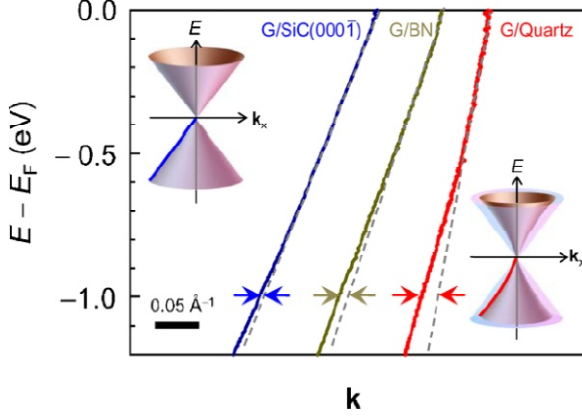


Fig. 8. Experimental $E_2(k_0+\kappa)$ dispersions for graphene on SiC(000 $\bar{1}$), BN, and quartz. Insets exhibit changing in the graphene Dirac cones when going from weak (left) to strong (right) interaction with substrate. Adapted from Ref. 55.

The total low-energy electronic spectrum of the graphene six pairs is described [49] as

$$\begin{aligned} E_1(k_0 + \kappa) &= E^0 - \left(\frac{\hbar p_0}{m} \right) \kappa, \\ E_2(k_0 + \kappa) &= E^0 + \left(\frac{\hbar p_0}{m} \right) \kappa. \end{aligned} \quad (7)$$

Here E^0 and k_0 are the Fermi energy and quasiparticle momentum at K (K') points while E_1 and E_2 spectra are related to the conducting and valence bands, respectively. Detailed description of parameter $\hbar p_0/m$ is given in Ref. 49. Eqs. (7) are well similar to those related to Dirac's massless fermions due to which the low-energy quasiparticles in the vicinity of K (K') points (Dirac points later) can formally be described by the Dirac-like Hamiltonian

$$\hat{H} = \hbar v_F \begin{pmatrix} 0 & k_x - ik_y \\ k_x + ik_y & 0 \end{pmatrix} = \hbar v_F \boldsymbol{\sigma} \cdot \mathbf{k}, \quad (8)$$

where \mathbf{k} is the quasiparticle momentum, $\boldsymbol{\sigma}$ is the 2D Pauli matrix for pseudospins and the k -independent Fermi velocity v_F plays the role of the speed of light. The equation is a direct consequence of graphene's crystal symmetry that involves honeycomb hexagonal lattice [51]. Owing to this specific electron band structure, graphene was attributed to the Dirac material and until now has remained a 'solid-state toy' for relativistic quantum mechanics [52-54]. Since the graphene massless Dirac fermions move with the Fermi velocity $v_F \approx 10^6 \text{ ms}^{-1}$, it is possible to mimic and observe quantum relativ-

istic phenomena, even those unobservable in high energy physics, on table-top experiments at much lower energies due to small value of the v_F/c ratio. Thus, a quite satisfactory consistence between theoretical predictions and experimental observations has allowed speaking about the observation of Dirac fermions in graphene. Taking them as physical reality, one has suggested a specific engineering of different Dirac fermions by modulating their Fermi velocity when attaching graphene to different substrates [55]. As seen in Fig. 8, an impressive changing of v_F from $1.15 \cdot 10^6 \text{ ms}^{-1}$ to $2.46 \cdot 10^6 \text{ ms}^{-1}$ is observed when substituting SiC(000 $\bar{1}$) substrate by quartz.

7. CHARACTERISTICS OF THE DIRAC CONE SPECTRA

Dirac cones are specific crystal symmetry effect that suits any flat (even quasiflat) hexagonal arrangements of atoms similar to the honeycomb lattice that provide hexagonal BZ. Actually, the Dirac-fermion-like behavior of electronic states were observed for monolayers of silicon atoms on Ag(111) surface (voluntarily attributed to 'silicene' species [56] (see detailed discussion of the reality and virtuality of silicene in Ref. 57)). Similar behavior was predicted for higher tetrels of group 14 elements - germanene and stanene [58]. Particular attention should be given to a new class of artificial 'molecular graphenes' that mimic honeycomb lattice structure. One of such 'molecule' was synthesized using individually placed carbon monoxide molecules on Cu(111) surface [59]. A completed 'flake' of the molecular graphene is shown in topographic form in Fig. 9a, demonstrating a perfect internal honeycomb lattice and discernible edge effects at the boundaries. In spite of finite size of the structure obtained, due to which it should be attributed rather to 'molecular graphene' than to 'graphene crystal', as seen in Fig. 9b, two energy cones are characteristic for the energy band structure near the Fermi level. Estimations showed that the crystal-like behavior is well conserved when the molecule size is of 20 nm or more. The other quite peculiar ability to create artificial graphene-like structure utilizes an optical honeycomb lattice to trap ultracold potassium atoms [60]. Dirac-cone-like band structure is reproduced in this system as well. This optical method of creating the honeycomb lattice suggests large possibility to investigate factors influencing the Dirac cones structure. Thus, by tuning the anisotropy of the lattice, the locations of the Dirac points may be shifted. When the anisotropy reaches a certain limit,

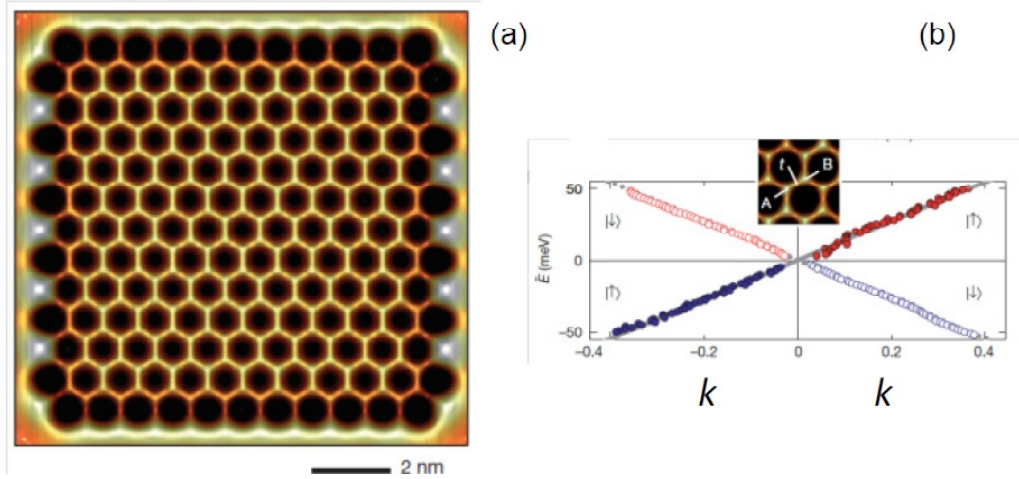


Fig. 9. (a) Constant current topograph of molecular graphene-like lattice composed of 1549 CO molecules. (b) Linearly dispersing quasi-particles revealed by the conductance spectra, plotted individually for sublattice A (filled circles: pseudospin $s_z=+1/2$) and sublattice B (open circles: pseudospin $s_z=-1/2$), measured at locations t illustrated in the inset. Adapted from Ref. 59.

the Dirac points merge and annihilate, while the evidence supporting the existence of a theoretically predicted topological phase transition was observed.

A number of theoretical suggestions on the Dirac-graphene-like structure is quite impressive. It covers virtual silicene, germanene, stanene (see review [61] and references therein), hydrogenated borophene [62] and arsenene [63]. All the Dirac species are described by hexagon packing of two-atom primitive cells. However, 'the primitive cell' may be considerably complicated as it takes place in the case of s-triazines with primitive cells composed of either C_6N_6 or $C_{12}N_6$, and $C_{24}N_6H_{12}$ molecular compositions [64], graphitic carbon nitride (GCN) with $C_{14}N_{10}$ as a primitive cell [65], beautiful hexagon patterned lace of $NiC_8S_2H_4$ molecules [66], the FeB_2 monolayer with graphene-like boron sheet [67], an impressive number of MXenes [68] (a new class of inorganic 2D compounds [69]), just appeared new compound InSe [70] and so forth (see review [71] and references therein). The conservation of the hexagon packing of primitive cells mentioned above protects the presence of Dirac cones in the electronic spectra of all the species.

Virtually all the Dirac spectra discussed were calculated not paying attention to if the studied system is open- or closed-shell one and exploiting closed-shell formalism. Only calculations related to GCN $C_{14}N_{10}$ [65] and metal-organic framework (MOF) with primitive cell $Ni_2C_{24}S_6H_{12}$ [66] were obtained taking into account that electrons with α and β spins are correlated and separated in space. The approach immediately revealed spin-polarization of the electronic spectra just doubling the band number and

combining them in α and β sets, which is clearly seen for GCN and the mentioned MOF in Fig. 10. The configurations of the relevant primitive cells are shown under the spectra. Both primitive cells contain even number of valence electrons, $N_\alpha = N_\beta$ so that in the two cases there are no unpairing free spins since total spin density is zero. The authors explain the observed spin polarization from a chemical bonding analysis and attributed it to reducing the anti-bonding characteristics and density of states at Fermi level [65].

However, it is quite reasonable to suggest an alternative explanation and connect the obtained spin polarization caused by p_z odd electron correlation with open-shell character of the electronic system of both cells caused by the breaking of spin symmetry. Actually, as shown in Fig. 10e, in view of the UHF formalism, the molecule $C_{14}N_{10}H_4$, which perfectly mimics the GCN primitive cell, is open-shell one with the total number of effectively unpaired electrons $N_D = 5.34$ that are distributed as local spins over nitrogen and carbon atoms with average N_{DA} fractions of 0.285 ± 0.001 and 0.145 ± 0.003 , respectively (see Fig. 10f). Therefore, the open-shell character of solid GCN and MOF as well as spin polarization of their electronic band are just a manifestation of the relevant emergent phenomena caused by symmetry breaking (SB). The spin-polarized band structure of GCN and MOF shown in Fig. 10, presents the first symmetry-breaking emergent related to dand spectra of 2D solids. As seen in the figure, the spin polarization is well pronounced through over both BZs while at K points the Dirac spectra still remain gapless (see insert in Fig. 10a).

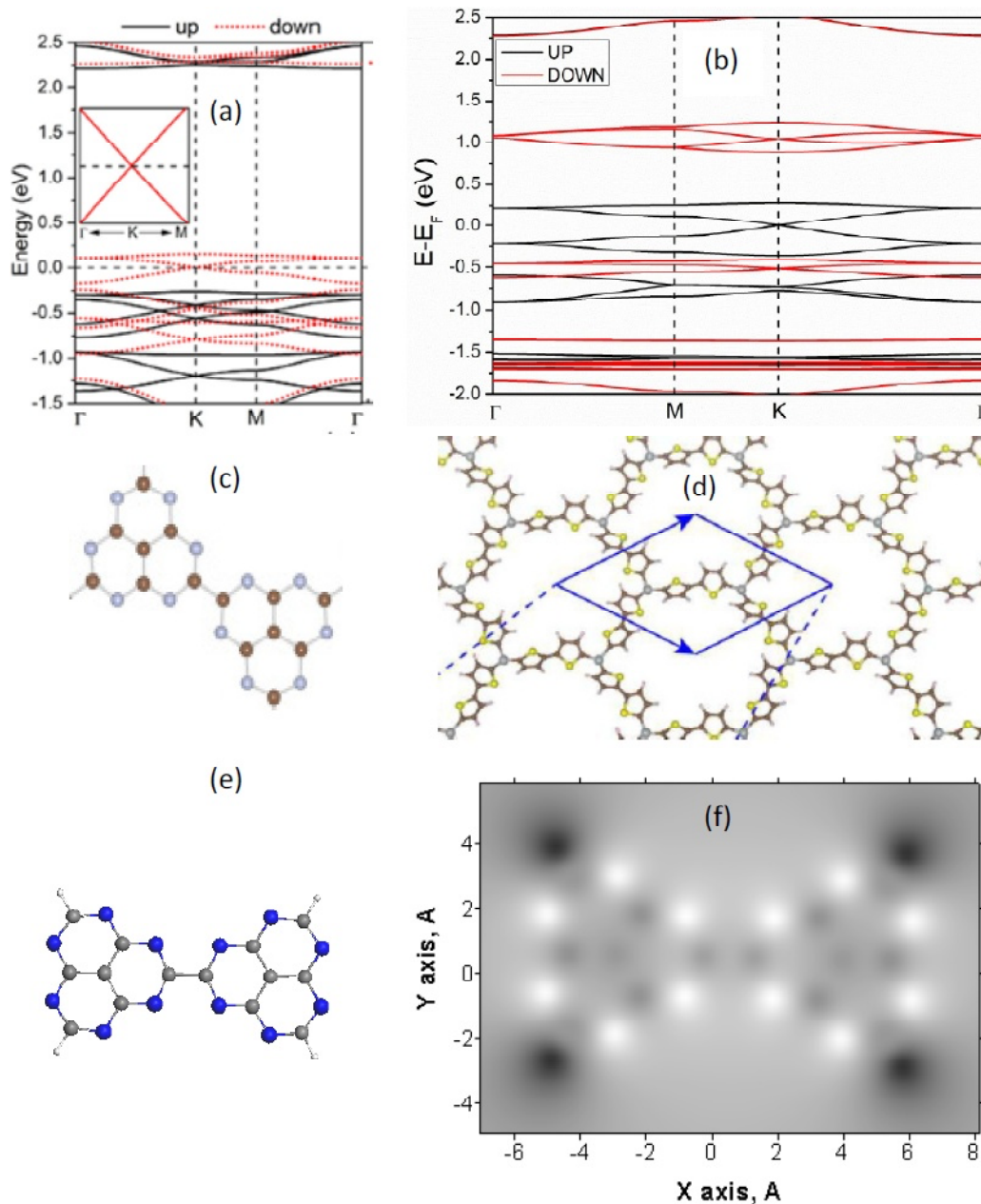


Fig. 10. Spin-polarized band structure and primitive cell of GCN $C_{14}N_{10}$ (a) and (c) and MOF $Ni_2C_{24}S_6H_{12}$ (b) and (d). Adapted from Refs. 65 and 66, respectively. Equilibrium structure (e) and the ACS N_{DA} image map of local spin distribution (f) of the $C_{14}N_{10}H_4$ molecule. UHF AM1 calculations.

Evidently, the feature is still caused by the hexagon packing of the molecules and is well resistant to the discussed symmetry-breaking. As for graphene, the relevant results concerning the band structure of the crystal are still in future while Fig. 11 presents the UHF emergent analogue related to a selected number of spinorbitals of the (5,5) NGr molecule. A comparison of RHF and UHF results allows exhibiting correlation effects related to the studied open-shell molecule. The degeneracy of the RHF solution is caused by both high spatial (D_2) and spin symmetry of the molecule. As seen in the figure,

when going from RHF to UHF formalism the UHF orbitals become clearly split into two families related to α and β spins. The splitting value is different for different orbitals ranging from 0.02 eV to 1.12 eV, thus defining the range to be expected for crystal band splitting as well.

8. DIRAC FERMIONS AND TOPOLOGICAL NON-TRIVIALITY OF GRAPHENE

As shown above, spin polarization does not affect the cones touching in the Dirac spectrum shown in

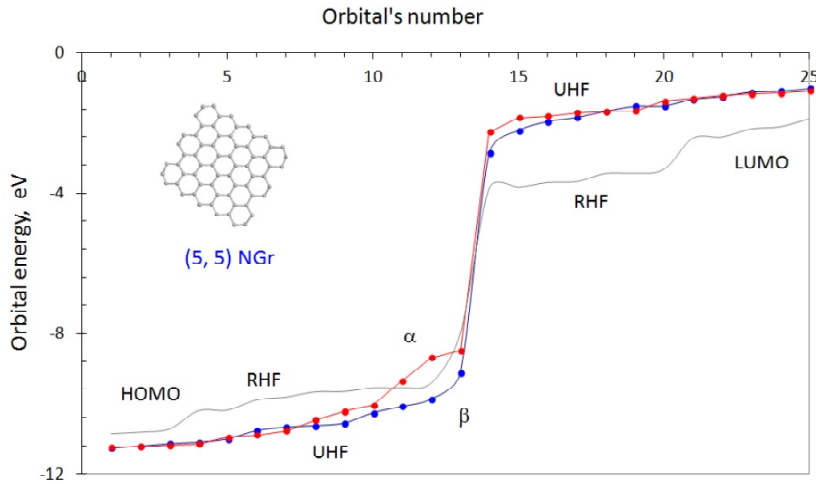


Fig. 11. Energies of 25 spinorbitals in the vicinity of HOMO-LUMO gap of (5,5) NGr molecule with bare edges. UHF AM1 calculations.

Fig. 7 (see insert in Fig. 10a). A scrupulous study revealed that the gapless structure can be violated by SOC only [51]. At the same time, the intrinsic SOC of graphene is quite negligible due to which the gap emergence in its Dirac spectrum should be hardly expected. However, the electron correlation, which, as we saw, is significant, generates a dynamical SOC (see Ref. 72 and references therein) due to which it might be possible to expect some relativistic features, observable at even negligible intrinsic SOC but at a significant electron correlation. The first potential effect concerns the splitting of the Dirac spectrum. To examine if such a splitting is observable experimentally, the team of Novoselov and Geim performed a particular investigation of how close one can approach the Dirac point [73]. It was shown that the approach value depends on the quality and homogeneity of samples, on the resolution of experimental equipment, on temperature, and so forth. The best value δE related to free standing sample constitutes ~ 1 meV at 4K, thus establishing that there is no bandgap in graphene larger than 0.5 meV and that a combined SOC effect is less the value. Nevertheless, the finding does not disprove the existence of SOC as such, which may be important in the case of other effects, more sensitive to weak SOC. One of such potential effects concerns the topological non-triviality of graphene.

Actually, electron correlation and SOC are crucial characteristics of the topological non-triviality of 2D solids. This question has been clear since the very time of the Dirac topological insulator (TI) discovery [74]. In the case of graphene, negligible SOC and complete ignorance of the electron corre-

lation, caused by calculations performed in the restricted formalism, were major obstacles to a serious discussion of this issue. However, the topological non-triviality covers a large spectrum of different topological states and phases involving both ideal Dirac TIs (or quantum spin Hall insulators – QSHIs) and other topological issues such as correlated topological band insulators, interaction-driven phase transitions, topological Mott insulators and fractional topological states [72] interrelation between which is determined by that one between correlation effects and SOC. Fig. 12 presents a phase diagram of topological states characteristic for 2D graphene-like honeycomb lattice (known as Kane-Mele model [51]) in relative coordinates of correlation energy (U) and SOC (λ_{SO}) specific for the Hubbard model [72]. As seen in the figure, in the limit case $\lambda_{SO}=0$, the relevant 2D structures should be attributed to either semimetal (SM) or quantum spin liquid (QSL) and antiferromagnetic Mott insulator (AFMI) with Heisenberg order (xyz), depending on the correlation energy. The SOC increasing transforms SM solid and QSL into QSHI at a rather large scale of the correlation energy variation. When the value achieves the critical one shown by the solid line, the QSHI transforms into AFMI with easy plane order (xy). In the limit case $U=0$, the solid should behave as QSHI at all λ_{SO} .

Concerning graphene, recent estimation of $U/t \approx 1.6$ [75] allows placing graphene far below the border with the QSL and AFM phases and attributing it to the SM phase if $\lambda_{SO} = 0$. However, the doubtless presence of the correlation of graphene p_z electrons causes unavoidable breaking of Kramers pairs of spinors [44], which violates the time-reversal sym-

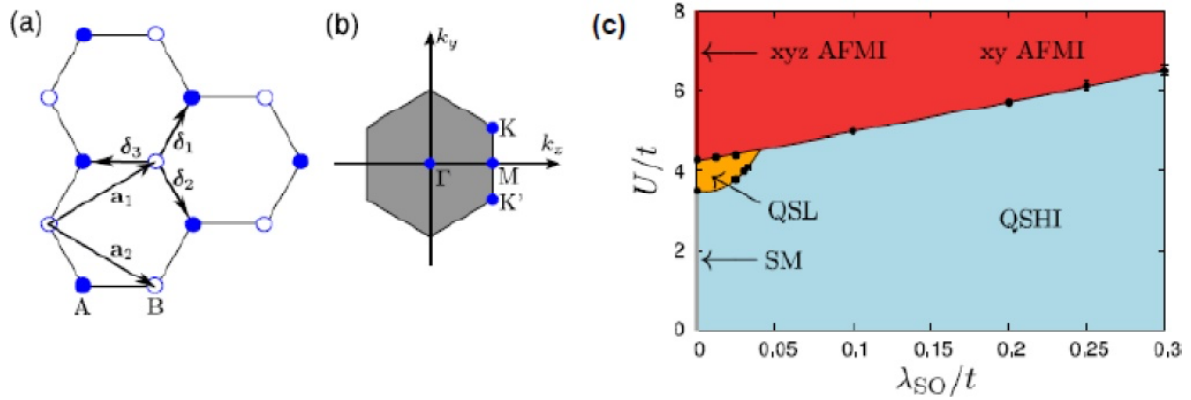


Fig. 12. (a) Kane-Mele model of the honeycomb lattice consisted of two sublattices A, B. (b) The hexagonal first Brillouin zone contains two nonequivalent Dirac points K and K'. (c) Phase diagram of the half-filled Kane-Mele-Hubbard model from quantum Monte Carlo simulations. Adapted from Ref. 72.

metry, on the one hand, and stimulates the origin of dynamic SOC, on the other [72]. The findings shift graphene along the λ_{SO}/t axis in the depth of the QSHI phase thus providing a vivid topological non-triviality of graphene that might be revealed by not only the SOC-stimulated energy gap splitting. One of such topological effects may have a direct bearing to peculiarities of graphene magnetism.

Referring to fundamental concepts on emergent physics [1-5], it is quite reasonable to suggest that topological non-triviality as well as magnetism and superconductivity belong to emergent phenomena. However, this aspect of graphene physics has not been clarified so far despite some issues concerning symmetry breaking were studied [76,77]. Apparently, the restricted TB formalism, used in the dominant majority of theoretical studies, might be one of the reasons of the issue gap. At the same time, definitely disclosed emergent phenomena in graphene chemistry convincingly evidence that phenomena of this type should be characteristic for graphene physics as well. We will try to prove the expectations analyzing peculiar magnetic and superconductive behavior of graphene. To the greatest extent, common chemical (molecular) and physical (crystal) roots of graphene emergents are manifested in the species magnetism.

9. MOLECULAR ESSENCE AND TOPOLOGICAL CHARACTER OF GRAPHENE MAGNETISM

9.1. General features of experimental observations

Repeatedly controlled extended graphene sheets are diamagnetic and magnetic response from large

samples was empirically obtained only after either, say, heavy irradiation by proton beams or chemical modification (hydrogenation, oxidation and so forth) of graphite and/or graphene (see [78] and references therein). Thorough analysis, performed in each case, allowed excluding the impurity origin of these features and attributing them to graphite/graphene itself, albeit induced by either micro- and/or nanostructuring of samples or by defects of different topology created in due course of chemical modification (see some examples [79-82]). It is important to mention that practically in all the cases a ferromagnetic response at room temperature was observed for graphene species with zero total spin density.

Another scenario concerns magnetic graphene of a paramagnetic behavior [81-83] recorded after either fluorination or bombarding graphene laminates consisting of 10-50 nm sheets by protons. The treatment provided the rupture of double C=C bonds inducing 'spin-half paramagnetism' in graphene. In both cases, the magnetization is weak and is characterized by one spin per approximately 1,000 carbon atoms. The ratio indicates that, actually, the after-treatment magnetic crystal structure differs from the pristine one and the difference concerns the unit cell that becomes $\sim 33/2$ times larger than the previous one. Besides, the unit cell contains one additional spin thus lifting the spin multiplicity to doublet. Therefore, introduced adatoms and point defects cause a magnetic nanostructuring of the pristine crystal but with non zero spin density.

A doubtless confirmation that nanostructuring of graphene sheets plays a governing role in magnetization was obtained in the course of specifically configured experiments [84,85]. In both cases the

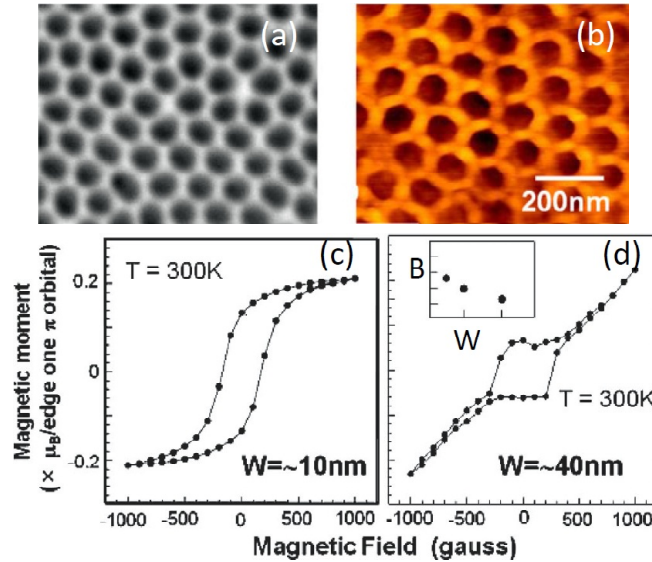


Fig. 13. (a) SEM image of nanoporous alumina template with mean pore diameter ~ 80 nm and mean inter-pore spacing $W \sim 20$ nm. (b) AFM image of graphene nanopore array formed by using (a) as an etching mask for the sample one-side hydrogenation. (c) and (d) Magnetization of monolayer graphene nanopore arrays at $W \sim 10$ nm and 40 nm. Inset presents the dependence of the residual magnetization of graphene webs on their width W . Adapted from Ref. 84.

matter is about meshed graphene or graphene in pores that were formed by either fully hydrogenated (oxidized) graphene discs in the first case or MgO nanoparticles in the second. A view on the sample and obtained results related to the first case can be obtained by looking at Fig. 13. A large graphene sheet is put on porous alumina template (see Fig. 13a). The sample was subjected to either one-side hydrogenation or oxidation through alumina pores thus leaving graphene webs between the pores untouched. The web width W in a set of alumina templates differed from 10 to 50 nm. Ferromagnetic response of the webs at room temperature is presented in Figs. 13b and 13c at different web widths and inset in Fig. 13c discloses the width dependence more clearly. In the second case, chemically modified dark disks in Fig. 13a were substituted with MgO nanoparticles a set of which was covered by CVD grown graphene tissue [85]. The web width between the particles constituted ~ 10 nm. The magnetic response from the sample is similar to that presented in Fig. 13b while the signal from much larger pieces ~ 100 nm of technical graphene (reduced graphene oxide [86]) was a few times less.

Therefore, nanosize occurrence and size-dependence, on the one hand, and high-temperature ferromagnetic character, on the other, are two peculiar features of zero-spin-density graphene magnetism. Evidently, the former concerns the magnetization magnitude and is associated with molecular essence of graphene while the latter is relevant to

the magnetism grounds and applies to its physics thus revealing the molecular-crystalline dualism of graphene once more.

9.2. Magnetic behavior of graphene molecules

Zero-spin-density graphene implies the absence of free spins since graphene belongs to species for which $N_\alpha = N_\beta$. Usually such magnetic species were attributed to 'singlet magnets' (in terms of closed-shell approximation) and their magnetization was associated with the effect of the second order of perturbation theory (PT) implying the mixture of the singlet ground state with higher lying states of higher spin multiplicity. If the mixture is caused by the application of magnetic field, the effect is known as van Vleck magnetization [87]. However, graphene is an open-shell species due to which its singlet ground state has already been spin-mixed due to p_z odd electron correlation. As well, since the difference between RHF and UHF formalisms is well described as PT second order effect [88], the spin contamination occurs originally and there is no need to apply the van Vleck effect for the magnetism explanation. The magnetization ability of graphene has been already ensured by its electronic system.

The observation of the PT second order contributions strongly depends on the energy denominator among other factors. For covalent species, triplet states are the main contributors due to which

the energy denominator is $2|J|$, where J is the exchange integral that determines the energetic dependence of pure spin states in terms of the Heisenberg Hamiltonian $H_{\text{ex}} = JS(S+1)$. The integral is usually referred to as magnetic coupling constant [89]. A correct computation of the constant is quite complicated. Happily, about four decades ago L. Noodleman suggested a simple expression for the value determination for open-shell molecules [90]. Then he introduced term of broken-spin-symmetry approximation, which in the light of the current discussion means the attribution of the magnetic behavior of molecules to emergent phenomena. According to Noodleman's approach,

$$J = \frac{E^U(0) - E^U(S_{\text{max}})}{S_{\text{max}}^2}. \quad (9)$$

Here, $E^U(0)$ and $E^U(S_{\text{max}})$ are energies of the UHF singlet and the highest-spin-multiplicity state, the latter corresponding to the S_{max} -pure-spin state. Thus obtained value is widely used and once attributed to molecular magnetism showed [91] that measurable magnetization response can be fixed if $|J| \leq |J_{\text{crit}}|$, where empirically estimated J_{crit} is 10^{-2} - 10^{-3} kcal/mol. Basing on the molecular essence of graphene magnetism, let us look which J values can be expected for graphene molecules (webs, ribbons, and so forth).

As seen in Table 1, J values show a significant size-dependence gradually decreasing by the absolute magnitude when the size grows. This dependence can be obviously interpreted as the indication of strengthening the electron correlation thus exhibiting the collective character of the event. The finding is expected to lay the foundation of peculiar size-effects for properties that are governed by these parameters, first of which can be addressed to molecular ferrodiamagnetism. The diamagnetic behavior is provided by σ electrons while the ferromagnetic contribution is obviously related to odd p_z ones. As mentioned earlier, the primitive cell of graphene crystal, which determines magnetic properties of ideal crystal, involves two atoms joint by one C=C bond of a benzenoid unit. Estimation of $|J|$ value for ethylene and benzene molecule with stretched C=C bonds up to 1.42 Å in length gives $|J|$ values of 13 kcal/mol and 16 kcal/mol, respectively. Despite ethylene and benzene molecules do not reproduce the unit cell exactly, a similar $|J|$ constant of the cell is undoubted. Owing to this, any magnetization outside diamagnetism is negligible due to which crystalline graphene should demonstrate the diamagnetic behavior only. To provide a

remarkable 'ferrodiamagnetism' means a drastic decrease of the magnetic constant $|J|$. While it is impossible for regular crystal, graphene molecules are more labile. Shown in Table 1, the least $|J|$ of 0.3 kcal/mol is still large to provide a recordable magnetization of (15,12) NGr molecular magnet, but the tendency is quite optimistic. Supposing the quantity to be inversely proportional to the number of odd electrons, it is possible to estimate the electron number which would satisfy $|J_{\text{crit}}|$ of 10^{-2} - 10^{-3} kcal/mol, which gives us $N \sim 10^5$ e.

For rectangular NGr, N odd electrons are supplied by N carbon atoms that, according to [92], is determined as

$$N = 2(n_a n_z + n_a + n_z). \quad (10)$$

To fit the needed N value, the indices n_a and n_z should be of hundreds, which leads to linear sizes of the NGr from a few units to tens of nm. The estimation is rather approximate, but it, nevertheless, correlates well with experimental observations of the ferromagnetism of activated carbon fibers consisting of nanographite domains of ~2 nm in size [93] as well as with the data related to meshed graphene [84,85] discussed earlier. The maximum effect was observed at the web distance of 20 nm [84] after which the signal gradually decreased when the width increased. The behavior is similar to that obtained for fullerene oligomers [94], which led to the suggestion of a scaly mechanism of nanostructured solid state magnetism of the polymerized fullerene C_{60} that was confirmed experimentally.

The said above highlights another noteworthy aspect of the graphene magnetism attributing the phenomenon to size-dependent ones. The latter means that the graphene ferromagnetism is observed for nanosize samples only, moreover, for samples whose linear dimensions fit a definite interval, while the phenomenon does not take place at either smaller or bigger samples outside the critical region. Actually, an individual benzenoid unit (and benzene molecule) is only diamagnetic. When the units are joined to form a graphene-like benzenoid cluster, effectively unpaired electrons appear due to weakening the interaction between p_z odd electrons followed by stretching C=C bonds which causes these electrons correlation. The correlation accelerates when the cluster size increases, which is followed with the magnetic constant $|J|$ decreasing until the latter achieves a critical value that provides a noticeable fixation of the spin mixing of the cluster ground state. Until the enlargement of the clus-

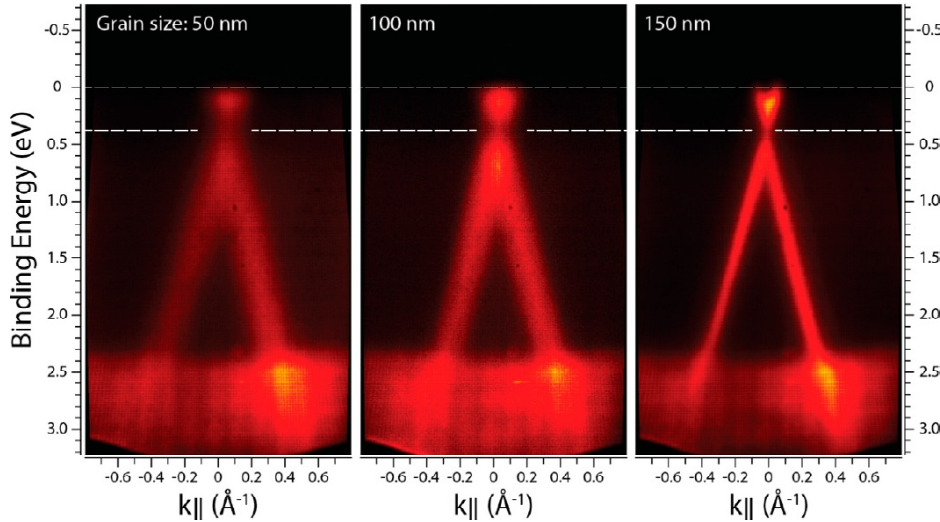


Fig. 14. Dirac's cones of continuous graphene film with average grain sizes of 50, 100, and 150 nm at the K point of graphene Brillouin zone obtained by ARPES mapping. Fermi energy is settled to zero. Adapted from Ref. 95.

ter size does not violate a molecular (cluster-like) behavior of odd electrons, the sample magnetization will grow. However, as soon as the electron behavior becomes spatially quantized, the molecular character of the magnetization will be broken and will be substituted by that one determined by the electron properties of the primitive cell. Critical size parameters, controlling quantization of molecular properties obviously depends on the kind of quasiparticles to be considered. Addressing graphene ferrmagnetism, evidently it is Dirac fermions that control the quantizing and their mean free path l_{fm} determines the critical size parameter: when the cluster size exceeds l_{fm} the spatial quantization quenches the cluster magnetization.

Happily, just recently experimental data related to the study of size dependence of both the linearity of the fermion low-energy band $E_{fm}(k)$ within the Dirac cones in the vicinity of the Fermi level and the shape of the spectrum were published. Fig. 14 presents a set of $E_{fm}(k)$ spectra related to a polycrystalline graphene sample consisting of grains different in size [95]. As seen in the figure, quantizing is well supported in grains of 150 nm, starts to be distorted in grains of 100 nm and is remarkably violated for grains of 50 nm. A considerable broadening of the spectrum in the last case allows putting the upper bound for l_{fm} around 50 nm. A comparable l_{fm} value of ~ 20 nm follows from the data related to CO-hexagon structure [59].

Obviously, the transition from localized to quantized state is not abrupt. Thus at the web width $W = 40$ nm the residual magnetization only halves the maximum value at 20 nm (see inset in Fig. 13c)

and continuous approaching to zero may cover quite a large web width. Actually, in the case of MgO nanoparticles [85], magnetization of rGO flakes with width ~ 100 nm constitutes $\sim 20\%$ of the value at the the reference web width of 10 nm. Nevertheless, the molecules linear size is evidently the governing factor for the magnitude of ferrodiamagnetism of pristine graphene.

9.3. High-temperature ferromagnetic topological insulating phase of graphene

If discussed in the previous section allows understanding when magnetic behavior of graphene becomes measurable, it does not answer question why the behavior is ferromagnetic and still exists at room and higher temperatures. Actually, it is difficult to expect ferromagnetism from the species with zero total spin density in the ground state. Additionally, molecular magnetism is usually observed at quite low temperatures [91] and its fixation at room temperature looks highly unexpected. At the same time there are physical objects for which high-temperature ferromagnetism is a characteristic mark. Thus, we come again to peculiar Dirac materials known as TIs [74]. As shown in the previous section, quite considerable electron correlation and small, but available, intrinsic-dynamic SOC allow attributing graphene to weak QSHI. However, there is still the question if, the topological non-triviality is relevant to both crystalline and molecular graphene. Fortunately, a convincing answer to this question has been received just recently [96]. It was demonstrated

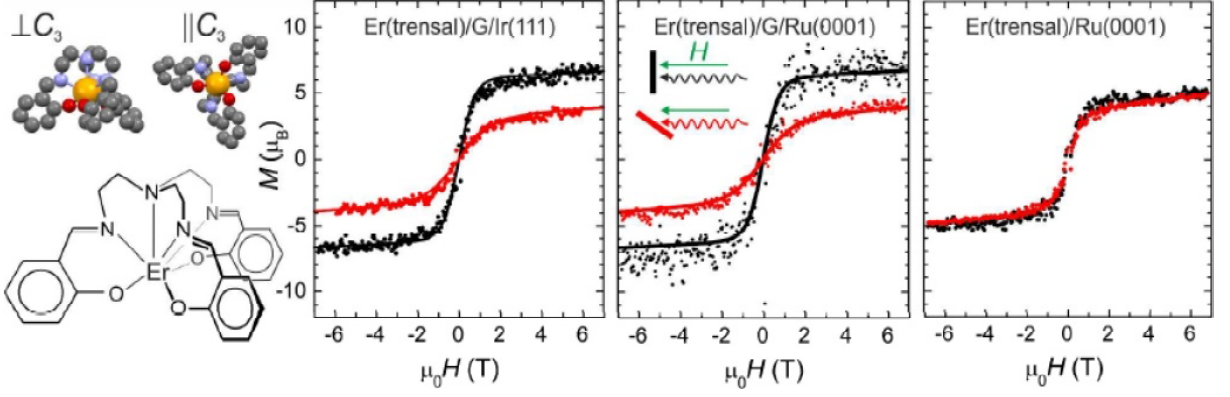


Fig. 15. Structural views and scheme of the molecular magnet Er(trensal). Coloring: orange: Er; blue: N; red: O; grey: C; H atoms are omitted for clarity. From left to right: magnetization curves at normal (black) and grazing (red) orientation of magnetic field with respect to the substrate surface. Adapted from Ref. 99.

experimentally that a macroscopic TI phase could emerge in a granular conductor composed of an assembly of tunnel coupled TI nanocrystals of dimension $\sim 10 \text{ nm} \times 10 \text{ nm} \times 2 \text{ nm}$. Evidently, the behavior is of a general nature due to which graphene molecules can be considered as nanosize TIs.

According to the UHF consideration, graphene presents a honeycomb structure of carbon atoms with local spins distributed over them. The spin values are not integer and are determined by the relevant N_{DA} values forming an image ACS map similar to that presented in Fig. 10f. Evidently, the exchange interaction between these local spins is responsible for the magnetic behavior of graphene. To determine the type of the behavior, let us use the formalism suggested for describing the magnetic impurities on the surface of a topological insulator [97]. In the presence of magnetic impurity or local spins, the main Hamiltonian, describing the TI band structure in the form of Eq. (8), is substituted by new one

$$H = v_F (\mathbf{k} \times \hat{\mathbf{z}}) \cdot \boldsymbol{\sigma} - H_{ex}, \quad (11)$$

where v_F is the Fermi velocity, $\hat{\mathbf{z}}$ is the surface unit normal, $\boldsymbol{\sigma}$ is the Dirac electron spin and

$$H_{ex} = \sum_r J_z s_z(\mathbf{r}) S_z(\mathbf{r}) + J_{xy} (s_x S_x + s_y S_y). \quad (12)$$

Here $S_i(\mathbf{r})$ is the spin of a magnetic impurity located at \mathbf{r} , $s_i(\mathbf{r}) = \psi^*(\mathbf{r}) s^i \psi(\mathbf{r})$ is the spin of the surface electrons and J_z and J_{xy} are the coupling parameters. When the impurity spin is polarized in z direction the second term in Eq. (12) disappears. As every magnetic impurity opens a local gap in its vicinity, one may expect the system to be gapped everywhere, at least in the mean-field level. However, this is not necessarily true if the magnetization of magnetic impurities is non-uniform. Meeting

the problem and comparing the formation of magnetic domain wall and ferromagnetic arrangement, the authors [97] came to the conclusion that magnetic impurities must be ferromagnetically coupled.

Sharing this viewpoint, a similar Hamiltonian H_{ex} was suggested to describe the Dirac-fermion-mediated ferromagnetism in a topological insulator [98]. The Hamiltonian H_{ex} reads

$$H_{ex} = J n_s \bar{S}_z \sigma_z. \quad (13)$$

Here σ_z is z -component of the electron spin and n_s is the areal density of localized spins with average z -component \bar{S}_z . J describes the exchange coupling between the z -components of the Dirac electron spin $\boldsymbol{\sigma}$ and the local spin \mathbf{S} , locking $\boldsymbol{\sigma}$ perpendicular to the momentum \mathbf{k} . Following the same conclusion that every local spin opens the gap and the system must be gapped everywhere one has to accept the necessity of a ferromagnetic configuration for local spins. Apparently, it is the consequence that explains ferromagnetic behavior of pure graphene samples.

Highly convincing evidence, strongly supporting suggestion that graphene is a typical TI, was received in the most recent [99]. Fig. 15 presents a molecular complex, presented by Er(trensal) single-ion magnets that was adsorbed on graphene/Ru(0001) and graphene/Ir(111) interfaces and on bare Ru(0001) substrate. On both interfaces, the molecules self-assemble into dense and well-ordered islands with their magnetic easy axes perpendicular to the surface. In contrast, on bare Ru(0001) the molecules are disordered exhibiting only weak directional preference of the easy magnetization axis. Accordingly, the ferromagnetic response is spin polarized in the two former cases while unpolarized

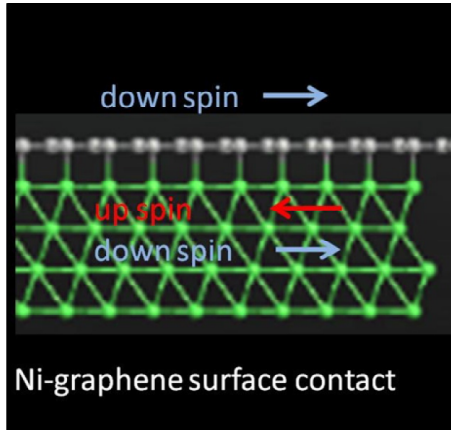


Fig. 16. Scheme of spin filtering at ferromagnetic metal/graphene interface. Adapted from Ref. 101.

in the case of Ru(0001) substrate and additionally twice less by magnitude. Therefore, topologically trivial bare ruthenium surface has no effect on the molecular impurity ordering while the addition of a graphene monolayer leads to ferromagnetic ordering of the impurity spins characteristic for topologically non-trivial substrates, which were discussed above. Not only ordering but enhancement of ferromagnetic response evidences the TI nature of the graphene component of the interfaces. Actually, the substitution of ruthenium by iridium has no additional effect so that all the observed peculiarities are caused by graphene layer. As for the response enhancement, $J_z = J_z(s_z)$ in the right-hand part of Eq. (13) acts as an effective magnetic field to magnetize the magnetic impurities. At the same time, J_z acts as the effective magnetic field to polarize the electron spin of TI. Obviously, such a double action of the exchange coupling leads to the enhancement of the magnetic response. When magnetic impurities form a continuous adlayer, additional enhancement should be expected due to the magnetic proximity effect (see one of the last publications [100] and references therein). Therefore, empirically confirmed graphene behaves as typical TI, which leads to a severe reconsideration of its physical properties discussed mainly without taking into account this important fact.

Since the submission of this paper, a few notable experimental works have appeared that remove the last doubts concerning the membership of graphene in the community of topological insulators. The first two are related to spin filtering observed in complex interfacial junctions FM/Gr/FM formed by a sandwich of ferromagnetic metals (FM) with single or multiple layer graphene inside [101,102]. The observed effect, common for both

cases, is schematically presented in Fig. 16. When monolayer (three layer) graphene is put on NiFe (Ni) FM (in Refs. 101 and 102, respectively) and covered by another FM, the transport of electrons with a particular spin orientation is occurred. This effect is well understood in light of the unique property of topological insulator implying the locking of electron spins to their momentum. Accordingly, one can expect introducing ferromagnetic order into a topological insulator system in places of contact with either magnetically ordered adsorbate layer, as it was in the case of the deposition of molecular magnets [99] (see Fig. 15), or underlying FM due to magnetic proximity effect [100]. In both cases, the interfacial ferromagnetism is a serious feature, greatly influencing the behavior of injected spins. Thus, it is an evident obstacle for an arbitrary transport of such spins, creating benefits for a particular spin orientation thus providing a spin filtering that was discussed above.

The next experimental discovery concerns another proximity-induced effect, namely, interfacial superconductivity, introduced by placing graphene monolayer on a superconductive $\text{Sr}_{1.85}\text{Ce}_{0.15}\text{TiO}_4$ crystal surface (see Fig. 17a). Three distinguishing fingerprints provided by scanning tunneling spectroscopy features dI/dV and characteristic for superconductive behavior, namely: V-shaped gaps, zero bias peaks (ZBPCs), and split ZBPCs – were observed when scanning the interface [103]. A typical view of ZBPCs scans is presented in Fig. 17b. A deep intrinsic connection between TI properties and superconductivity [74] convincingly evidences that both spin filtering and superconductivity is provided by the topological non-triviality of graphene. Important to note, that interfacial superconductivity is preserved at temperature, much higher than that of the superconductive substrate. A similar lifting of the temperature above the Curie point of the relevant ferromagnetic substrate is observed in the case of proximity-induced interfacial ferromagnetism [101,102]. Both temperature effects are typical for TIs.

It is interesting to look at superconductivity as a typical emergent effect [1-5]. From this viewpoint a deep similarity between UHF and Bardin, Cooper, and Schrieffer (BCS) equations [76] does not seem strange. If the two formalisms are of the same roots, it becomes evident that species, whose emergent phenomena become evident via UHF should be certainly prone to superconductivity under appropriate conditions. Apparently this very situation occurs with graphene.

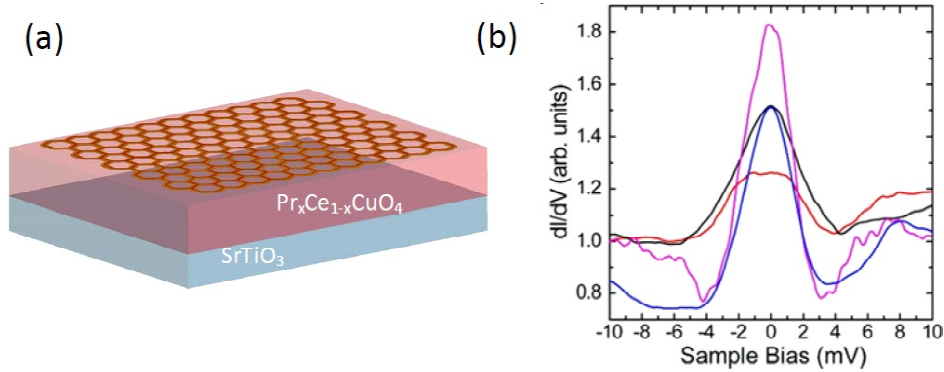


Fig. 17. (a) Scheme of superconductor/graphene interface. (b) Zero bias peaks scanned at different areas of the interface at $T=4.2\text{K}$. Adapted from Ref. 103.

10. COMMENTS ON CONVERTING GRAPHENE FROM SEMIMETAL TO SEMICONDUCTOR

Despite numerous extraordinary properties and huge potential for various applications, one of the greatest challenges in using graphene as an electronic material is the lack of a sizable bandgap. Accordingly, graphene is intrinsically a zero-gap QSHI, but a semimetal in the view of most. The gap absence significantly limits the use of graphene in many applications where semiconducting behaviour with a suitable bandgap are required. Researchers have been searching for effective ways to produce semiconducting graphene and have developed various methods to generate a bandgap. Despite extensive investigation in the laboratory, the production of semiconducting graphene is still facing many challenges. A detailed description of problems on the way as well as suggestions for their resolving is given in review [104]. Let us look at the problems from the viewpoint of obvious ‘underwater stones’ provided by emergents of graphene chemistry.

When categorizing methods to produce semiconducting graphene, three groups were classified: (1) morphological patterning of graphene sheets into nanoribbons, nanomeshes, or quantum dots to induce quantum confinement and edge effects; (2) chemical modification, doping, or surface functionalization of graphene to intentionally interrupt the connectivity of the π electron network; and (3) other methods, e.g., use of two graphene layers arranged in Bernal stacking (or AB stacking) to break the lattice symmetry, and applying mechanical deformation or strain to graphene.

Following this scheme, techniques of the first group meet problems concerning the basic edge property of the graphene molecule that is obviously a dangling-bond effect. Actually, cutting graphene

sheets into nanoribbons increases the number of dangling bonds and, consequently, the number of effectively unpaired electrons thus enhancing the ribbon radical properties. In its turn, the extra radicalization greatly promotes various chemical reactions at the ribbon circumference leading to significant and even sometimes drastic reconstruction of the pristine graphene structure. Inserting nanomeshes results in the same effect due to highly active periphery of the formed holes. Deposition of nanosize quantum dots strongly disturbs the graphene substrate changing C=C bond length distribution and thus causing the N_D growth if even not contributing by their own effectively unpaired electrons. Therefore, cutting and drilling create a big ‘edges problem’ and do not seem to be proper technologies for the wished transformation of the graphene electronic system.

Chemical modification of graphene is not only a subject of interesting chemistry but has been repeatedly suggested as an efficient tool for the semimetal-semiconductor transferring needed for high-performance electronics [10]. It should be noted that the suggestions are based on results of computational studies that concern pencil-drawn pictures of graphene fragments including those or other chemical modifiers artificially spread over graphene sheets (see, for example, Refs. 105 and 106). These and many other virtual structures, regularly distributed in space by applying periodic boundary conditions, exhibit electronic properties that are so badly needed for the application. However, the empirical reality is much less promising since so far a very scarce number of regularly chemically modified graphene structure has been obtained. And collective behavior of graphene effectively unpaired electrons, protesting against any response localization, is the main reason for the failure.

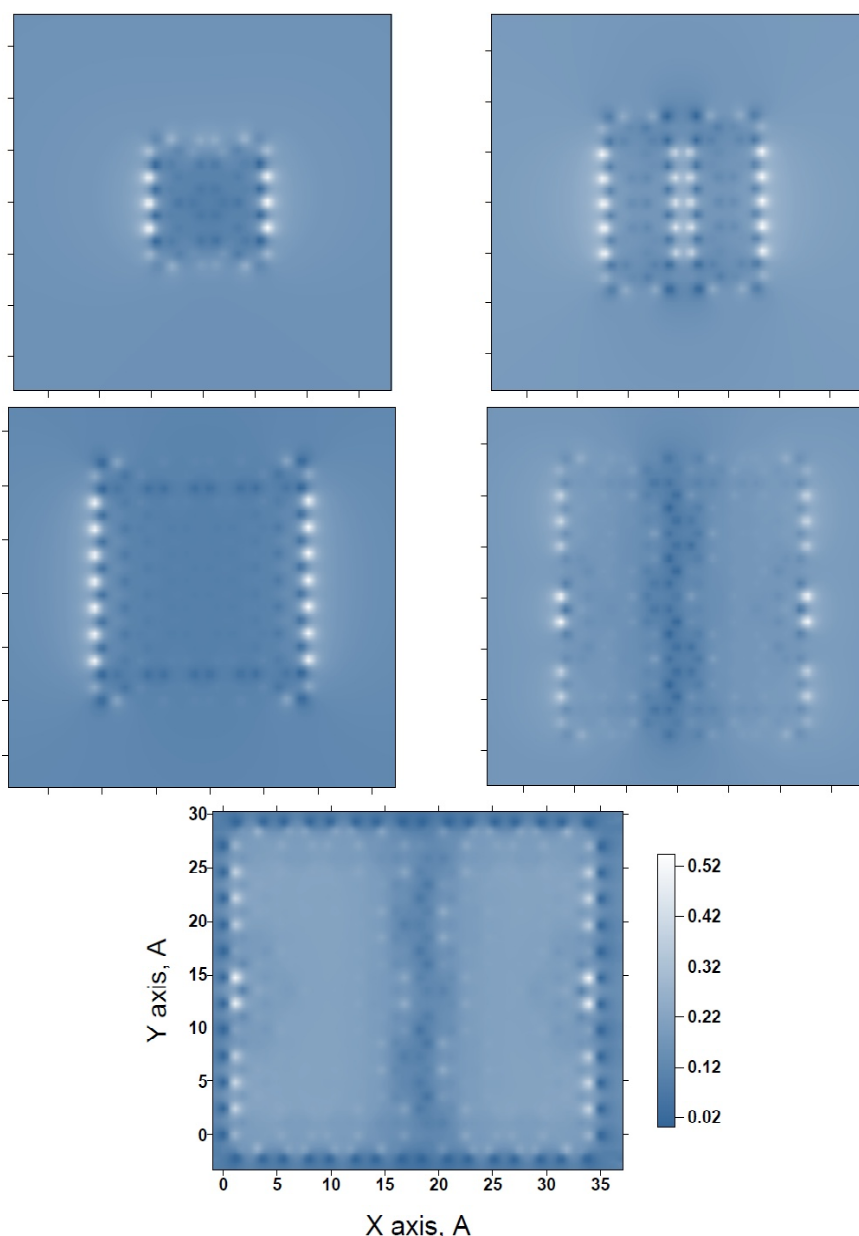


Fig. 18. ACS N_{DA} image maps over atoms of the (5,5), (7,7), (9,9), (11,11), and (15,12) NGr molecules with monohydrogen terminated edges. All the images are given in the same space and N_{DA} scales shown on the bottom. UHF AM1 calculations.

The wished regular structures of chemically modified graphene are related to graphene polyderivatives that are formed with the participation of carbon atoms on the basal plane. However, as was shown in Section 4, reactions at the circumference precede those at the basal plane. Moreover, the latter cannot begin until the former are completed. In the predominant majority of the studied cases, the completion of the circumference reactions means the completion of framing of the studied molecules. A thorough study of the circumference reactions has disclosed a very exciting feature: the framing of graphene molecules promotes the molecule crack-

ing. Fig. 18 presents a set of ACS N_{DA} image maps related to monohydrogen terminated (H_1 -terminated below) NGr molecules of different size. The ACS maps of all the pristine molecules are of identical pattern characteristic for the (11,11) NGr molecule shown in Fig. 2 just scaled according to the molecule size. As seen in the figure, the ACS maps of H_1 -terminated polyderivatives show a peculiar two-part division related to (15,12) ($3.275 \times 2.957 \text{ nm}^2$) and (11,11) ($2.698 \times 2.404 \text{ nm}^2$) NGr molecules in contrast to the maps of (9,9) ($1.994 \times 2.214 \text{ nm}^2$), (7,7) ($1.574 \times 1.721 \text{ nm}^2$), and (5,5) ($1.121 \times 1.219 \text{ nm}^2$) NGr molecules. Apparently, the finding dem-

onstrates the ability of graphene molecules to be divided when their linear size exceeds 1-2 nm. The cracking of pristine graphene sheets in the course of chemical reaction, particularly, during oxidation, was repeatedly observed. A peculiar size effect was studied for graphene oxidation [107] and fluorination [108]. During 900 sec of continuous oxidation, micrometer graphene sheets were transformed into ~1 nm pieces of graphene oxide. Obviously, the tempo of cracking should depend on particular reaction conditions, including principal and service reactants, solvents, temperature, and so forth (see [109,110]). Probably, in some cases, cracking can be avoided. Apparently, this may depend on particular conditions of the inhibition of the edge atoms reactivity. However, its ability caused by the inner essence of the electron correlation is an imminent threat to the stability and integrity of the final product.

In some cases, the cracking is not observed when graphene samples present membranes fixed over their perimeter on solid substrates. Therewith, the reactivity of circumference atoms is inhibited and the basal plane is the main battlefield for the chemical modification. Still, as in the case of circumference reactions considered earlier, the highest ACS retains its role as a pointer of the target carbon atoms for the subsequent reaction steps. However, the situation is much more complicated from the structural aspect viewpoint. Addition of any modifier to the carbon atom on the basal plane is accompanied by the $sp^2 \rightarrow sp^3$ transformation of the valence electrons hybridization so that for regularly packed chemical derivatives the benzenoid skeleton of pristine graphene should be substituted by the cyclohexanoid one related to the formed polyderivatives. When benzene molecules and, subsequently, benzenoid units are monomorphic, cyclohexanes, and thus cyclohexanoid units, are highly heteromorphic. Not very big difference in the conformers free energy allows for coexisting cyclohexanoids of different structure thus making the formation of a regular structure a rare event. Actually, the regular crystalline-like structure of a graphene polyhydride, known as graphane, was obtained experimentally under particular conditions only when hydrogenating fixed graphene membranes accessible to hydrogen atoms from both sides [111]. In the same experiment, fixed membranes (ripples over substrate) accessible to hydrogen atoms from one side showed irregular amorphous-like structure. The empirical findings were supported by computations based on the consideration of stepwise hydrogenation of fixed and free standing membranes

accessible to hydrogen atom from either two or one sides [35].

As shown above, it is possible to proceed with chemical modification of graphene within the basal plane only after a complete inhibition of high chemical activity of atoms at the circumference. Despite the N_{DA} values within the area are much less than at a bare circumference, as seen in Fig. 2b, they still constitute ~0.3-0.1 that is quite enough to maintain active chemical modification. However, the reality drastically differs from the wished chemical patterning of graphene sheets whose virtual image present the final product of the patterning as regular carpets similar to flowerbeds of French parks. The reality is more severe and closer to designs characteristic of English parks. The matter is that the collective of effectively unpaired electrons, which strictly controls the chemical process at each step, has no means by which to predict the modifier deposition sites many steps forward. And it is clear why. Each event of the modifier deposition causes an unavoidable structure deformation due to local $sp^2 \rightarrow sp^3$ transformation in the place of its contact with graphene. The relaxation of the deformation, as was seen in Fig. 6, extends over a large area, which, in turn, is accompanied by the redistribution of C=C bond lengths. Trying to construct a patterning, it is impossible, while not making calculations, to guess at what exactly carbon atom will concentrate the maximum reactivity, highlighting the latter as a target atom to the next deposition. Therefore, even two simultaneous depositions cannot be predicted, not to mention such complex as quantum dots or nanoribbons. That is why a wished regular chemical patterning of graphene basal plane exists only in virtuality. The real situation was studied in detail in the case of graphene hydrogenation [112], exhibiting the gradual filling of the basal plane with hydrogen at random. Final products of the addition reactions on basal planes of graphene strongly depend on the addends in use. None of the regular motives was observed in all the cases in the course of stepwise reactions.

To overcome the difficulties and to achieve a wished goal of regular distribution of modifiers over graphene basal plane, it is necessary to transform the graphene sheet into a peculiar chemical template with regularly distributed regioselectivity over the plane atoms. This can be done by a regular buckling of the carbon skeleton. Actually, due to governing role of the interatomic distance related to C=C bonds in the correlation of p_z odd electrons, any deformation, which causes stretching (contraction) of these bonds greatly affects the electron

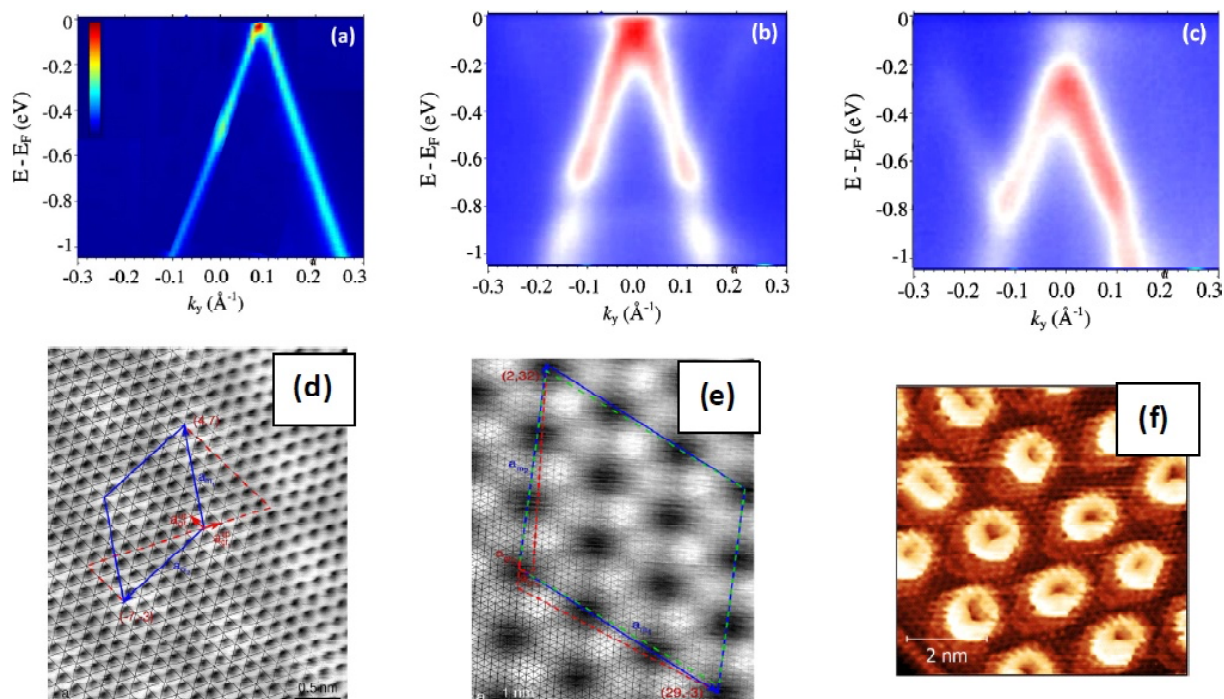


Fig. 19. Dirac cones of periodically patterned graphene; ARPES (top) and STM (bottom) images. (a, d). Multilayer C-face graphene film on the 6H SiC surface, ARPES at $T=6$ K; adapted from Ref.114. (b, e) Graphene/Ir(111) interface; adapted from Ref.115 (b) and Ref. 114 (e). Blue and red lines in panels (d) and (e) mark lattice vectors of the upper graphene lattice and moiré superlattice, respectively. (c, f). Graphene/Ir(111) interface saturated with atomic hydrogen at a sample temperature of 645K.; adapted from Ref. 115.

behavior thus exhibiting the buckle tops as places with enhanced (reduced) ACS [18]. Evidently, a buckle-reactor with regular distribution of the regioselective areas is easily generated when graphene sheet is placed over a regularly patterned substrate formed by, say, nanosize pyramids [113] or metal nanoparticles deposited on a substrate. Template of the same kind takes place at one-layer adsorption of carbon atoms on metal surfaces, which results in the formation of the interface with a peculiar moiré structure (see [114] and references therein). Because of the lattice mismatch between graphene and the metal surface, the graphene sheets form an incommensurate phase that exhibits moiré patterns caused by graphene buckling. The buckling tops become the sites of preferable attaching by any addends thus promoting regular chemical modification of graphene.

The latter installation has been realized just recently by the group of L. Hornekaer, which resulted in the controlled opening of the gap via hydrogenation of graphene while previously placed on the Ir(111) surface [115], after six years from the first attempt, described above [112]. The interface graphene/Ir(111) is characterized by a moiré structure with hexagonal super-cell. The hydrogen clusters bind graphene

exclusively on specific regions on the superlattice thus promoting the conservation of the Dirac cone spectrum of these pristine graphene (see Fig. 19) while shifting it down and opening the band gap. The technique opens a large way of various combinations, which, complemented by bi- and multilayers adsorption and application of mechanical deformation or strain, attributes the problem of the gap opening to amazing spin mechanochemistry of graphene.

11. CONCLUSION

Concluding this story about the unique properties of graphene, we can not dwell on yet one more unique feature of graphene as a subject of scientific research. The latter concerns publications on a subject, the majority of which are devoted to computational results. Never before did theoretical and computational works take so much space in the natural sciences. Among the references, there is a big number of works whose conclusive remarks herald the creation of either new graphene-like material or suggestion of new methods to affect graphene properties in a wished way and so forth. The vast majority of these studies were performed by using easily accessible closed-shell versions of DFT applied to

pencil-made models. To the delight of computationists, the obtained solutions are spin and time symmetric, there are no problems related to emergent phenomena, results can be quickly obtained and published. The only nuisance spoiling this gracious picture is that these results are not about real graphene which is full of exclusiveness, universality, emergency provided by its spin and time symmetry breaking. If this were not, there would not be peculiar chemistry, mechanochemistry, topochemistry, and biomedicine of graphene, plasticity, ferromagnetism and superconductivity, topological non-triviality, peculiar optical properties, and so forth.

The recognition of broken symmetry as a leading factor towards its universality and the understanding of the emergent character of graphene properties open a new paradigm for graphene application. Not graphene itself, but graphene as a smart companion material may be more attractive and more easily implemented in various devices thus approaching the term of high performance applications. This conclusion is well supported by exclusive interfacial phenomena concerning ferromagnetism, spin filtering and superconductivity discussed in the paper. Firstly revealed in physics, the interfacial phenomena evidently are of general motif of graphene emergents and can be found in different branches of graphene science. Thus, one of such issues can be attributed to graphene geology. The matter concerns a unique structure of nanosize quartz inclusions embedded in shungite carbon (the latter presents natural technical graphene (reduced graphene oxide) [86]). As occurred, the quartz, usually greatly variable by chemical composition, full-of-defect structure and size from one deposit to the others, is of unique perfect crystalline structure and practically of the same size in different deposits of shungite [116]. Apparently, quartz/shungite interface, subordinated to emergent regularities of graphene chemistry, played the governing role in the course of this composite mineral generation. There are grounds to believe that similar phenomena might take place in graphene biomedicine where graphene involving interfaces are often met.

ACKNOWLEDGEMENTS

This publication was prepared with the support of the "RUDN University Program 5-100".

REFERENCES

[1] P.W. Anderson // *Science* **177** (1972) 393.

- [2] R. B. Laughlin and D. Pines // *PNAS* **97** (2000) 28.
- [3] R. B. Laughlin // *Rev. Mod. Phys.* **71** (1999) 863.
- [4] *Emergent Phenomena in Correlated Matter*, ed. by E. Pavarini, E. Koch and U. Schollwöck (Forschungszentrum Jülich and the German Research School for Simulation Sciences, 2013, Jülich).
- [5] C. Yannouleas and U. Landman // *Rep. Prog. Phys.* **70** (2007) 2067.
- [6] P-O. Löwdin // *Adv. Chem. Phys.* **2** (1958) 209.
- [7] Y. Kitagawa, T. Saito, Y. Nakanishi, Y. Kataoka, T. Matsui, T. Kawakami, M. Okumura and K. Yamaguchi // *J. Phys. Chem. A* **113** (2009) 15041.
- [8] J.P. Coe and M. Paterson // *Int. J. Quant. Chem.* **116** (2016) 1772.
- [9] Y. Cui, I.W. Bulik, C.A. Jiménez-Hoyos, T.M. Henderson and G.E. Scuseria // *J. Chem. Phys.* **139** (2013) 154107.
- [10] K.S. Novoselov, V.I. Fal'ko, L. Colombo, P.R. Gellert, M.G. Schwab and K. Kim // *Nature* **490** (2012) 192.
- [11] E.F. Sheka // *Adv. Quant. Chem.* **70** (2015) 111.
- [12] E.F. Sheka, *Fullerenes: Nanochemistry, Nanomagnetism, Nanomedicine, Nanophotonics* (CRC Press, Taylor & Francis Group, Boca Raton London New York, 2011).
- [13] G. Blanquart // *Int. J. Quant. Chem.* **115** (2015) 796.
- [14] H. Fucutome // *Int. J. Quant. Chem.* **20** (1981) 955.
- [15] K. Takatsuka, T. Fueno and K. Yamaguchi // *Theor. Chim. Acta* **48** (1978) 175.
- [16] V.N. Staroverov and E.R. Davidson // *Chem. Phys. Lett.* **330** (2000) 161.
- [17] E.F. Sheka and V.A. Zayets // *Russ J Phys Chem* **79** (2005) 2009.
- [18] E.F. Sheka // *Int. J. Quant. Chem.* **114** (2014) 1079.
- [19] L. Gross, F. Mohn, N. Moll, B. Schuler, A. Criado, E. Guitián, D. Peña, A. Gourdon, and G. Meyer // *Science* **337** (2012) 1326.
- [20] A. Mistry, B. Moreton, B. Schuler, F. Mohn, G. Meyer, L. Gross, A. Williams, P. Scott, G. Costantini and D.J. Fox // *Chem. Eur. J.* **21**(2014) 2011.
- [21] N. Pavliček, A. Mistry, Z. Majzik, N. Moll, G. Meyer, D.J. Fo and L. Gross // *Nature Nanotech.* (2017) **12** (2017) 308.

- [22] J. van der Lit, M.P. Boneschanscher, D. Vanmaekelbergh, M. Ijäs, A. Uppstu, M. Ervasti, A. Harju, P. Liljeroth and I. Swart // *Nat. Commn.* **4** (2013) 2023.
- [23] V.A. Zayets, *CLUSTER-Z1: Quantum-Chemical Software for Calculations in the s,p-Basis* (Institute of Surface Chemistry Nat Ac Sci of Ukraine, Kiev, 1990).
- [24] E.F. Sheka // *Int. J. Quant. Chem.* **112** (2012) 3076.
- [25] E.F. Sheka // *Int. J. Quant. Chem.* **107** (2007) 2803.
- [26] E.F. Sheka // *J. Struct. Chem.* **47** (2006) 593.
- [27] J.H. Warner, Y.-C. Lin, K. He, M. Koshino and K. Suenaga // *Nano Lett.* **14** (2014) 6155.
- [28] K. Nakada and M. Fujita // *Phys. Rev. B* **54** (1996) 17954.
- [29] A.S. Barnard and I.K. Snook // *Modelling Simul. Mater. Sci. Eng.* **19** (2011) 054001.
- [30] M. Acik and Y.J. Chabal // *Jpn. J. Appl. Phys.* **50** (2011) 070101.
- [31] P.C. Mishra and A. Yadav // *Chem. Phys.* **402** (2012) 56.
- [32] L.S. Ang, S. Sulaiman and M.I. Mohamed-Ibrahim // *Monatsh. Chem.* **144** (2013) 1271.
- [33] R. Hoffmann // *Ang. Chem. Int. Ed.* **52** (2013) 93.
- [34] I. Mayer // *Int. J. Quant. Chem.* **29** (1986) 73.
- [35] E.F. Sheka and N.A. Popova // *J. Mol. Model.* **18** (2012) 3751.
- [36] E. Sheka and N. Popova // *Phys. Chem. Chem. Phys.* **15** (2013) 13304.
- [37] W. Liu // *Mol. Phys.* **108** (2010) 1679.
- [38] K. Dyall and K. and Faegri, *Introduction to Relativistic Quantum Chemistry* (Oxford University Press, New York, 2007).
- [39] M. Reiher and A. Wolf, *Relativistic Quantum Chemistry: The Fundamental Theory of Molecular Science*, 2nd Edition, (Willey, 2014).
- [40] P.-O. Löwdin and I. Mayer // *Adv. Quant. Chem.* **24** (1992) 79.
- [41] C.M. Marian, In: *Reviews in Computational Chemistry*, Vol. **17**, ed. by K.B. Lipkowitz and D.B. Boyd (2001), p. 99.
- [42] Y.S. Kim, S.Y. Lee, W.S. Oh, B.H. Park, Y.K. Han, S.J. Park and Y.S. Lee // *Int. J. Quant. Chem.* **66** (1996) 91.
- [43] M. Nakano, J. Seino and H. Nakai // *Int J Quantum Chem.* (2017) **117** (2017) 25356.
- [44] L. Bučinský, M. Malček, S. Biskupič, D. Jayatilaka, G.E. Büchel and V.B. Arion // *Comp. Theor. Chem.* **1065** (2015) 27.
- [45] E.F. Sheka, N.A. Popova and V.A. Popova, // *Physics Uspekhi*, DOI: 10.3367/UFNe.2017.11.038233.
- [46] E.F. Sheka, In: *Carbon Materials: Chemistry and Physics* **7**, ed. by Ali Reza Ashrafi et al. (2013), p. 137.
- [47] E.F. Sheka, *Spin Chemical Physics of Graphene* (Pan Stanford, Singapore, 2017).
- [48] P.R. Wallace // *Phys. Rev.* **71** (1947) 622.
- [49] J.C. Slonczewski and P.R. Weiss // *Phys. Rev.* **109** (1957) 272.
- [50] G. W. Semenoff // *Phys. Rev. Lett.* **53** (1984) 2449.
- [51] C. L. Kane and E. J. Mele // *Phys. Rev. Lett.* **95** (2005) 226801.
- [52] M.I. Katsnelson // *Materials Today* **10** (2007) 20.
- [53] A.K. Geim and K.S. Novoselov // *Nat. Mat.* **6** (2007) 183.
- [54] P. Kim, In: *Matiere de Dirac* (Seminaire Poincare XVIII, 2014), p. 1.
- [55] C. Hwang, D.A. Siegel, S.-K. Mo, W. Regan, A. Ismach, Y. Zhang, A. Zettl and A. Lanzara // *Sci. Rep.* **2** (2012) 590.
- [56] A. Kara, H. Enriquez, A.P. Seitsonen, L.C. Lew, Yan Voon, S. Vizzini, B. Aufray and H. Oughaddou // *Surf. Sci. Rep.* **67** (2012) 1.
- [57] E.F. Sheka // *Nanosyst. Phys. Chem. Math.* **7** (2016) 983.
- [58] R.W. Zhang, W.-X. Ji, C.W. Zhang, P. Li and P.J. Wang // *Phys. Chem. Chem. Phys.* **18** (2016) 28134.
- [59] K.K. Gomes, W. Mar, W. Ko, F. Guinea and H.C. Manoharan // *Nature* **483** (2012) 307.
- [60] L. Tarruell, D. Greif, T. Uehlinger, G. Jotzu and T. Esslinger // *Nature* **483** (2012) 302.
- [61] G.R. Bhimanapati, Z. Lin, V. Meunier, Y. Jung, J. Cha, S. Das, D. Xiao, Y. Son, M.S. Strano, V.R. Cooper, L. Liang, S.G. Louie, E. Ringe, W. Zhou, B.G. Sumpter, H. Terrones, F. Xia, Y. Wang, J. Zhu, D. Akinwande, N. Alem, J.A. Schuller, R.E. Schaak, M. Terrones and J.A. Robinson // *ACS Nano* **9** (2015) 11509.
- [62] L.-C. Xu, A. Du and L. Kou // *Phys. Chem. Chem. Phys.* **18** (2016) 27284.
- [63] C. Wang, Q. Xia, Y. Nie, M. Rahman and G. Guo // *AIP Advances* **6** (2016) 035204.
- [64] A. Wang, X. Zhang and M. Zhao // *Nanoscale* **6** (2014) 11157.

- [65] X. Zhang, A. Wang and M. Zhao // *Carbon* **84** (2015) 1.
- [66] L. Wei, X. Zhang and M. Zhao // *Phys. Chem. Chem. Phys.* **18** (2016) 8059.
- [67] H. Zhang, Y. Li, J. Hou, A. Du and Z. Chen // *Nano Lett.* **16** (2016) 6124.
- [68] C. Si, K.-H. Jin, J. Zhou, Z. Sun and F. Liu // *Nano Lett.* (2016) **16** (2016) 6584.
- [69] M. Naguib, V.N. Mochalin, M.W. Barsoum and Y. Gogotsi // *Adv. Mat.* **26** (2014) 992.
- [70] D.A. Bandurin, A.V. Tyurnina, G.L. Yu, A. Mishchenko, V. Zólyomi, S.V. Morozov, R.K. Kumar, R.V. Gorbachev, Z.R. Kudrynskiy, S. Pezzini, Z.D. Kovalyuk, U. Zeitler, K.S. Novoselov, A. Patané, L. Eaves, I.V. Grigorieva, V.I. Fal'ko, A.K. Geim and Y. Cao // *Nat. Nanotech.* **12** (2016) 203.
- [71] J. Wang, S. Deng, Z. Liu and Z. Liu // *Nat. Sci. Rev.* **2** (2015) 22.
- [72] M. Hohenadler and F.F. Assaad // *J. Phys.: Condens. Matter* **25** (2013) 143201.
- [73] A. S. Mayorov, D. C. Elias, I. S. Mukhin, S. V. Morozov, L. A. Ponomarenko, K.S. Novoselov, A.K. Geim and R. V. Gorbachev // *Nano Letters* **12** (2012) 4629.
- [74] *Topological Insulators: Fundamentals and Perspectives*, ed. by F. Ortmann, S. Roche, S.O. Valenzuela and L.W. Molenkamp (Wiley, 2015).
- [75] M. Schüler, M. Rösner, T.O. Wehling, A.I. Lichtenstein and M.I. Katsnelson // *Phys. Rev. Lett.* **111** (2013) 036601.
- [76] V. Bach, E. H. Lieb and J.P. Solovej // *Journ. Stat. Phys.* **76** (1994) 3.
- [77] D. Zheng, G-M. Zhang and C. Wu // *Phys. Rev. B* **84** (2011) 205121.
- [78] O.V. Yazyev // *Rep. Prog. Phys.* **73** (2010) 05650130.
- [79] P. Esquinazi, D. Spemann, R. Hohné, A. Setzer, K. H. Han and T. Butz // *Phys. Rev. Lett.* **91** (2003) 227201.
- [80] M. Sepioni, R.R. Nair, S. Rablen, J. Narayanan, F. Tuna, R. Winpenny, A.K. Geim, A.K. and I.V. Grigorieva // *Phys. Rev. Lett.* **105** (2010) 207205.
- [81] R.R. Nair, M. Sepioni, I.-L. Tsai, O. Lehtinen, J. Keinonen, A.V. Krasheninnikov, T. Thomson, A.K. Geim and I.V. Grigorieva // *Nat. Phys.* **8** (2012) 199.
- [82] A.Y.S. Eng, H.L. Poh, F. Sanek, M. Marysko, S. Matejkova, Z. Sofer and M. Pumera // *ACS Nano* **7** (2013) 5930.
- [83] R.R. Nair, I.-L. Tsai, M. Sepioni, O. Lehtinen, J. Keinonen, A.V. Krasheninnikov, A.H. Castro Neto, M.I. Katsnelson, A.K. Geim and I.V. Grigorieva // *Nat. Commn.* **4** (2013) 2010.
- [84] K. Tada, J. Haruyama, H. X. Yang, M. Chshiev, T. Matsui and H. Fukuyama // *Phys. Rev. Lett.* **107** (2011) 217203.
- [85] G. Ning, C. Xu, L. Hao, O. Kazakova, Z. Fan, H. Wang, K. Wang, J. Gao, W. Qian and F. Wei // *Carbon* **51** (2013) 390.
- [86] E.F. Sheka // *Int. J. Nanomat. Nanotech. Nanomed.* **3** (2017) 7.
- [87] J.H. Van Fleck, *The Theory of Electric and Magnetic Susceptibilities* (Oxford, 1932).
- [88] I. Hubač and P. Čàrski // *Int. J. Quant. Chem.* **24** (1983) 141.
- [89] C. Adamo, V. Barone, A. Bencini, R. Broer, M. Filatov, N. M. Harrison, F. Illas, J.P. Malrieu and I. de P.R. Moreira // *Journ. Chem. Phys.* **124** (2006) 107101.
- [90] L. Noodleman // *J. Chem. Phys.* **74** (1981) 5737.
- [91] O. Kahn, *Molecular Magnetism* (VCH, New York, 1993).
- [92] X. Gao, Z. Zhou, Y. Zhao, S. Nagase, S.B. Zhang and Z. J. Chen // *Phys. Chem. A* **112** (2008) 12677.
- [93] T. Enoki and Y. Kobayashi // *J. Mat. Chem.* **15** (2005) 3999.
- [94] E.F. Sheka, V.A. Zayets and I.Ya. Ginzburg // *J. Exp. Theor. Phys.* **103** (2006) 728.
- [95] C.T. Nai, H. Xu, S.J.R. Tan and K.P. Loh // *ACS Nano* **10** (2016) 1681.
- [96] A. Banerjee, O. Deb, K. Majhi, R. Ganesan, D. Sen and P. S. A. Kumar // *Nanoscale* **9** (2017) 6755.
- [97] Q. Liu, C.-X. Liu, C. Xu, X.-L. Qi and S.-C. Zhang // *Phys. Rev. Lett.* **102** (2009) 156603.
- [98] J.G. Checkelsky, J. Ye, Y. Onose, Y. Iwasa and Y. Tokura // *Nature Phys.* **8** (2012) 729.
- [99] J. Dreiser, G.E. Pacchioni, F. Donati, L. Gragnaniello, A. Cavallin, K.S. Pedersen, J. Bendix, B. Delley, M. Pivetta, S. Rusponi and H. Brune // *ACS Nano* **10** (2016) 2887.
- [100] F. Katmis, V. Lauter, F.S. Nogueira, B.A. Assaf, M.E. Jamer, P. Wei, B. Satpati, J.W. Freeland, I. Eremin, D. Heiman, P. Jarillo-Herrero and J.S. Moodera // *Nature* **533** (2016) 513.
- [101] E.D. Cobas, O.M.J. van 't Erve, S.-F. Cheng, J.C. Culbertson, G.G. Jernigan, K. Bussman and B.T. Jonker // *ACS Nano* **10** (2016) 10357.

- [102] K.H. Khoo, W.S. Leong, J.T.L. Thong and S.Y. Quek // *ACS Nano* **10** (2016) 11219.
- [103] A. Di Bernardo, O. Millo, M. Barbone, H. Alpern, Y. Kalcheim, U. Sassi, A.K. Ott, D. De Fazio, D. Yoon, M. Amado, A.C. Ferrari, J. Linder and J.W.A. Robinson // *Nat. Commun.* **8** (2017) 14024.
- [104] G. Lu, K. Yu, Z. Wen and J. Chen // *Nanoscale* **5** (2013) 1353.
- [105] L. A. Chernozatonski, P. B. Sorokin, E. E. Belova and J. Brüning // *JEPT Lett.* **85** (2007) 77.
- [106] N. Lu, Y. Huang, H.-B. Li, Z. Li and J. Yang // *J. Chem. Phys.* **133** (2010) 034502.
- [107] S. Pan and I.A. Aksay // *ACS Nano* **5** (2011) 4073.
- [108] N.A. Nebogatikova, I.V. Antonova, V.Ya. Prinz, I.I. Kurkina, V.I. Vdovin, G.N. Aleksandrov, V.B. Timofeev, S.A. Smagulova, E.R. Zakirova and V.G. Kesler // *Phys. Chem. Chem. Phys.* **17** (2015) 13257.
- [109] X. Wang, H. Bai and G. Shi // *J. Am. Chem. Soc.* **133**(2011) 6338.
- [110] J.H. Kang, T. Kim, J. Choi, J. Park, Y.S. Kim, M.S. Chang, H. Jung, K. Park, S.J. Yang and C.R. Park // *Chem. Mat.* **28** (2016) 756.
- [111] D.C. Elias, R.R. Nair, T.M.G. Mohiuddin, S.V. Morozov, P. Blake, M.P. Halsall, A.C. Ferrari, D.W. Boukhvalov, M.I. Katsnelson, A.K. Geim and K.S. Novoselov // *Science* **323** (2009) 610.
- [112] R. Balog, B. Jorgensen, L. Nilsson, M. Andersen, E. Rienks, M. Bianchi, M. Fanetti, E. Lægsgaard, A. Baraldi, S. Lizzit, Z. Slijivancanin, F. Besenbacher, B. Hammer, T.G. Pedersen, P. Hofmann and L. Hornekær // *Nature Mat.* **9**(2010) 315.
- [113] S.T. Gill, J.H. Hinnefeld, S. Zhu, W.J. Swanson, T. Li and N. Mason // *ACS Nano* **9** (2015) 5799.
- [114] M. Batzill // *Surf. Sci. Rep.* **67** (2012) 83.
- [115] J.H. Jørgensen, A.G. Cabo, R. Balog, L. Kyhl, M.N. Groves, A.M. Cassidy, A. Bruix, M. Bianchi, M. Dendzik, M.A. Arman, L. Lammich, J.I. Pascual, J. Knudsen, B. Hammer, P. Hofmann and L. Hornekær // *ACS Nano* **10** (2017) 10798.
- [116] R.V. Sadovnichiy, A.A. Mikhaylina, N.N. Rozhkova and I.S. Inina // *Proc. Karelian Sci. Center RAS* (2016) 73, In Russian, DOI: 10.17076/geo126.